Bioactive Materials 46 (2025) 1–20

Contents lists available at ScienceDirect

Bioactive Materials

journal homepage: www.keaipublishing.com/en/journals/bioactive-materials

An electrostatic encapsulation strategy to motivate 3D-printed polyelectrolyte scaffolds for repair of osteoporotic bone defects

Xiang Gao [a,1], Jirong Yang [b,c,1], Lingna Liu [a,1], Zilong Hu [a], Rui Lin [a], Lan Tang [b,c], Mei Yu [a], Zhiping Chen [a], Chongjian Gao [b], Min Zhang [a], Li Li [a,**], Changshun Ruan [b,c,*], Yanzhi Liu [a,***]

[a] Zhanjiang Key Laboratory of Orthopaedic Technology and Trauma Treatment, Key Laboratory of Traditional Chinese Medicine for the Prevention and Treatment of Infectious Diseases, Guangdong Key Laboratory for Research and Development of Natural Drugs, School of Pharmacy, School of Ocean and Tropical Medicine, The Affiliated Hospital, The Second Affiliated Hospital, Zhanjiang Central Hospital, Guangdong Medical University, Zhanjiang, 524037, China
[b] Research Center for Human Tissue and Organ Degeneration, Institute of Biomedicine and Biotechnology, Shenzhen Institute of Advanced Technology, Chinese Academy of Sciences, Shenzhen, 518055, China
[c] University of Chinese Academy of Sciences, Beijing, 100049, China

ARTICLE INFO

Keywords:
Bone regeneration
3D-printed scaffold
Electrostatic encapsulation
Salvianolic acid B
Bone targeting
Osteoporotic bone defects

ABSTRACT

Repair of osteoporotic bone defects (OBD) remains a clinical challenge due to dysregulated bone homeostasis, characterized by impaired osteogenesis and excessive osteoclast activity. While drug-loaded 3D-printed scaffolds hold great potential in the restoration of bone homeostasis for enhanced OBD repair, achieving the controlled release and targeted delivery of drugs in a 3D-printed scaffold is still unmet. Herein, we developed an electrostatic encapsulation strategy to motivate 3D-printed polyelectrolyte scaffolds (APS@P) with bone-targeting liposome formulation of salvianolic acid B (SAB-BTL). Benefiting from this strategy, SAB, an unstable and untargetable plant-derived osteogenic compound, was effectively encapsulated in APS@P, demonstrating stable and precise delivery with improved therapeutic efficacy. Owing to SAB-mediated bone homeostasis, APS@P significantly promoted angiogenesis and new bone formation while suppressing bone resorption, resulting in a significant 146 % increase in bone mass and improved microstructure compared to the OBD group. It was confirmed that the encapsulation of SAB into APS@P could promote the osteogenic differentiation of MSCs by stimulating Tph2/Wnt/β-catenin signaling axis, coupled with the stimulation of type H angiogenesis and the suppression of RANKL-mediate bone resorption, thereby enhance OBD repair. This study provides a universal platform for enhancing the bioactivity of tissue-engineered scaffolds, offering an effective solution for the efficient regeneration of osteoporotic bone.

1. Introduction

Osteoporosis leads to reduced bone mineral density and compromised bone microarchitecture, significantly increasing the risk of osteoporotic bone defects (OBD) [1]. Repairing OBD is particularly challenging due to disruptions in bone homeostasis, marked by excessive osteoclast activity and impaired osteogenesis [2]. This imbalance accelerates bone resorption, outpacing the body's capacity for bone regeneration and leading to insufficient repair. In clinical practice, the treatment of OBD continues to encounter several challenges. The standard treatment for OBD typically involves bone grafting—either autologous, allogeneic, or artificial bone substitutes—yet these approaches are limited by issues, such as donor-site morbidity, supply shortages, risks of immunogenicity and disease transmission. Another significant challenge in OBD treatment is achieving secure fixation. The treatment surgery must not only ensure the stability of implant materials, but also

* Corresponding author. Research Center for Human Tissue and Organ Degeneration, Institute of Biomedicine and Biotechnology, Shenzhen Institute of Advanced Technology, Chinese Academy of Sciences, Shenzhen, 518055, China.
** Corresponding author. Guangdong Key Laboratory for Research and Development of Natural Drugs, School of Pharmacy, School of Ocean and Tropical Medicine, Guangdong Medical University, Zhanjiang, 524037, China
*** Corresponding author. Zhanjiang Key Laboratory of Orthopaedic Technology and Trauma Treatment, Key Laboratory of Traditional Chinese Medicine for the Prevention and Treatment of Infectious Diseases, Zhanjiang Central Hospital, Guangdong Medical University, Zhanjiang, 524037, China
E-mail addresses: gy0661@163.com (L. Li), cs.ruan@siat.ac.cn (C. Ruan), liuyanzhi@gdmu.edu.cn (Y. Liu).
[1] These authors contributed equally: Xiang Gao, Jirong Yang, and Lingna Liu.

https://doi.org/10.1016/j.bioactmat.2024.12.007
Received 3 August 2024; Received in revised form 4 December 2024; Accepted 4 December 2024
Available online 7 December 2024

need to restore mechanical stability in the injured bone. To address this, bioinert materials like metals and polymethylmethacrylate (PMMA) are commonly used for fixation [3]. However, these materials lack bioactivity, which, combined with low bone mass in osteoporosis patients, often results in poor bone integration. This complicates the surgeon's efforts, leading to stress shielding, implant loosening, or even healing failure. Besides, anti-osteoporosis treatments, such as bisphosphonates, denosumab, and teriparatide, are often administered before OBD surgery treatment and may be continued long-term as adjunct therapies [4]. While these medications help increase and maintain bone mass, which is crucial for the success of OBD surgery and for reducing the risk of refracture, they lack targeted properties. As a result, these drugs struggle to reach the defect site and directly stimulate local bone regeneration. Consequently, these challenges render the outcomes of OBD treatment unpredictable, frequently involving delayed healing, nonunion, or periprosthetic fractures around implants [5–7]. As a result, novel approaches are urgently needed to overcome these challenges and achieve more effective repair of OBD.

Recent advancements in 3D-printed scaffolds have shown great potential for bone defect repair [8]. These scaffolds are precisely designed to provide mechanical support for promoting osteogenesis [9–11]. To enhance the osteogenic effect of these scaffolds, various bioactive factors such as BMP proteins [12], natural compounds [13,14], and metallic elements [15] have been incorporated into scaffolds to stimulate bone regeneration. Achieving the controlled release and targeted delivery of bioactive factors in a 3D-printed scaffold is critical to effective OBD repair. The most common method for incorporating bioactive factors into 3D-printed scaffolds involves simple physical mixing with bio-ink during printing process [16–21]. Although this approach is straightforward, it has several critical limitations. First, it often leads to a rapid burst release of the factors within the initial hours, leaving insufficient amounts for sustained tissue repair. Second, it fails to adequately protect drugs from degradation or oxidation, reducing their long-term efficacy. Finally, the non-specific release of these factors is unable to achieve targeted accumulation at the defect site, thereby limiting the effectiveness of bone regeneration. While significant progress has been made in bioactive factors-loaded 3D-printed scaffolds, current strategies still lack the ability to provide effective targeting and sustained bioactivity that both promotes osteogenesis and inhibits osteoclastogenesis, thereby enabling the effective repair of osteoporotic bone defects. Few bioactive factors are capable of simultaneously providing strong osteogenic stimulation and suppressing bone resorption. Overcoming these obstacles is crucial to develop effective treatments that can reconstruct osteoporotic bone defects.

Effective coupling of angiogenesis and osteogenesis is also crucial for successful bone repair [22]. Some natural product ingredients have shown promising potential in facilitating this process. Salvianolic acid B (SAB), a polyphenolic compound derived from *Salvia miltiorrhiza*, is a bioactive monomer known for its multi-target effects on both bone homeostasis and angiogenesis [23–26]. SAB enhances osteoblast proliferation, promotes neovascularization, and suppresses osteoclast activity [24,25,27–29]. It has been shown to protect endothelial progenitor cells from oxidative stress through the modulation of the Akt/mTOR/4EBP1, p38 MAPK/ATF2, and ERK1/2 signaling pathways [30]. SAB also promotes osteogenic differentiation in bone marrow-derived mesenchymal stem cells (BMSCs) by ERK signaling pathway while protecting against apoptosis caused by oxidative stress [31]. Additionally, SAB promotes osteogenic differentiation in human periodontal ligament cells via the Wnt/β-catenin pathway [32] and protects osteoblast function by modulating the keap1/Nrf2/ARE signaling pathway. Similar to SAB, salvianolic acid A [33] (Tanshinol), another constituent of *Salvia miltiorrhiza*, and also one of the molecules that constitute SAB, stimulates osteogenesis through pathways such as Wnt/β-catenin [34], TXNIP [35], and KLF15/PPARγ2 [36] signaling pathway. Moreover, salvianolate, which contains SAB as the main component, significantly suppresses hyperactive osteoclast activity by modulating the RANKL/OPG pathway in rheumatoid arthritis, highlighting its potential to inhibit bone resorption [29]. These combined osteogenic and anti-resorptive properties suggest that SAB can create a balanced microenvironment conducive to reversing dysregulated bone homeostasis, critical for repairing OBD. Given SAB's diverse biological activities, it emerges as a promising candidate for incorporation into 3D-printed scaffolds to achieve multifaceted therapeutic effects for OBD repair.

However, SAB's clinical utility is hindered by its low bone-targeting ability and susceptibility to oxidative degradation. To overcome these limitations, a bone-targeting liposomal delivery system (BTL) can be employed to enhance the bioavailability and site-specific delivery of SAB to bone tissue [37,38]. In previous studies, we developed a pyrophosphate-cholesterol-based BTL system that extended drug efficacy and therapeutic action in bone. This system was validated in both a glucocorticoid-induced delayed fracture mouse model [39] and a rabbit critical defect-induced nonunion model [40]. Building on these findings, the development of a bone-targeting liposomal formulation of SAB (SAB-BTL) holds significant potential to improve bone targeting, enhance therapeutic efficacy, and protect SAB from oxidative degradation, thus offering a promising approach for the treatment of OBD.

Here, we propose a novel strategy that combines electrostatic encapsulation with bone-targeting liposomes to enhance the osteogenic effects of SAB in a 3D-printed alginate/ε-polylysine (Alg/ε-PL) scaffold. SAB-BTL was developed using a pyrophosphate-cholesterol-based liposome delivery system designed to improve bone-targeting efficiency. These negatively charged SAB-BTL liposomes were then incorporated into a positively charged Alg/ε-PL ink to fabricate the APS@ scaffold. To further enhance the scaffold's sustained release performance, an additional positively charged ε-PL coating was applied, forming a robust electrostatic encapsulation layer. Thus, the SAB electrostatic encapsulated 3D-printed polyelectrolyte scaffold was fabricated (APS@P). *In vitro* experiments, the APS@P scaffold showed marked improvements in osteogenesis, angiogenesis, and cell migration. *In vivo* experiments, it demonstrated robust promotion of OBD repair by stimulating osteogenesis, supporting type H vessel formation, and suppressing osteoclast activity. These effects collectively contributed to improved local bone homeostasis, substantially enhancing the scaffold's regenerative capacity for OBD repair (Fig. 1). The combined strategy of electrostatic encapsulation and bone-targeting liposomes enables controlled, sustained, and precise drug delivery, and offers a universal platform for delivering bioactive factors that effectively promote bone regeneration and repair OBD.

2. Experiment section

2.1. Formulation and characterization of SAB-BTL

2.1.1. Formulation of SAB-BTL

Lecithin (600 mg, EMD Millipore Corporation, USA) and cholesterol (150 mg, Sigma-Aldrich, USA) were dissolved in methylene chloride (90 mL, Shanghai Aladdin Co., Ltd, China); SAB (120 mg, Tianjin Wanxiang Hengyuan Technology Co., Ltd., China) and cholesterol-pyrophosphate (300 mg, Xi'an Ruixi Biotechnology Co., Ltd., China) were dissolved in 15 mL PBS (pH 7.4) solution. The two solutions were combined and stirred using a magnetic stirrer for 10 min. The mixture became a homogeneous opalescent dispersion. To prevent oxidation during the formulation process, nitrogen gas was introduced as a protective measure. The reverse-phase evaporation method was then applied using a rotary evaporator, leading to the successful formation of a drug-loaded liposome emulsion as previously described [41]. The reverse-phase evaporation tends to form water-in-oil emulsions. The water phase carries the drug, and the organic phase is made up of lipids for forming the liposome bilayer. Under reduced pressure conditions, the organic solvent can be slowly evaporated, initially resulting in the conversion of the dispersion into a viscous gel and finally generating an aqueous suspension containing the drug-loaded liposomes. A mini-extruder

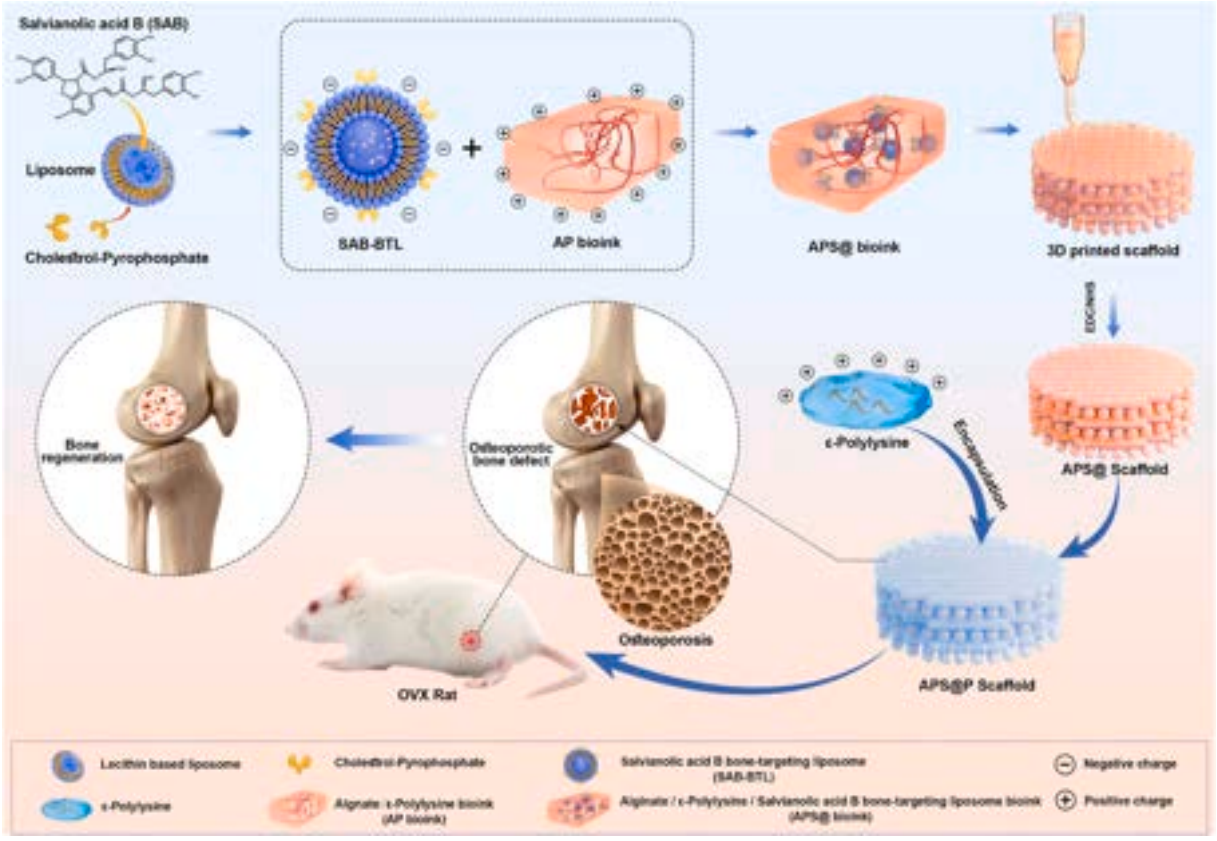

Fig. 1. Schematic illustration of the study design. A schematic illustration depicts the incorporation of SAB-BTL into an alginate/ε-polylysine 3D-printed scaffold (APS@P scaffold) for OBD regeneration. In this process, negatively charged SAB-BTL is formulated and integrated into a bioink composed of ε-polylysine and alginate polyelectrolyte (AP). This bioink is then used to fabricate the APS@ 3D scaffold. Within the scaffold, primary electrostatic interactions occur between the negatively charged SAB-BTL and the positively charged ε-polylysine. To further stabilize the scaffold, EDC/NHS is employed for crosslinking. Additionally, an electrostatic encapsulation coating step is performed by treating the scaffold with ε-polylysine, yielding the final APS@P scaffold. This scaffold is specifically engineered to enhance local bone homeostasis and improve regenerative capacity for repairing OBDs.

(Avanti Polar Lipids Inc., USA) with a 0.4 μm membrane and a 0.2 μm membrane (Whatman, UK) was utilized to adjust the liposome size to the desired liposomes. Subsequently, a sucrose (1 g/mL, Shanghai Aladdin Co., Ltd, China) solution was introduced into the liposome emulsion until the final sucrose concentration reached 20 %, with sucrose serving as the lyoprotectant. The ultimate liposome solution underwent freeze-drying to obtain SAB-BTL for subsequent experiments.

2.1.2. Particle size and zeta potential measurement of SAB-BTL

SAB and SAB-BTL were weighed and dissolved in PBS, and SAB/SAB-BTL solution were analyzed using a Nicomp 380 Z3000 analyzer (PSS, USA) for particle size and zeta potential (Table S1).

2.2. Fabrication of 3D-printed APS@P scaffolds

2.2.1. APS@ bio-ink preparation

Firstly, the Alg/ε-PL (AP) bioink was prepared as our previous described [42]. In detail, the Alg/ε-PL 1:1 bioink was prepared by adding Alg (low viscosity, Sigma-Aldrich, USA) to ε-PL (95 %, Macklin, China) solution with continually stirring until homogeneity. The ratio of alginate and ε-PL was based on the ratio of carboxyl groups of Alg and amino groups of ε-PL. When the amount of Alg was fixed to 4 g, the amount of ε-PL dissolved in 10 mL distilled water was 2.924 g. Then, the SAB-BLT was added to the ε-PL Alg/ε-PL bioink to obtain APS@ bioinks. The mass ratio (m) of AP to SAB-BTL was set at 2:1, 9:1, and 19:1, respectively. Different ratios of SAB-BTL were specified in Table S2. These bio-inks were used subsequently for the fabrication of 3D printed APS@P scaffolds.

2.2.2. Rheological test of APS@ bio-inks

A rheometer (MCR 302, Anton Paar, Austria) was utilized to conduct dynamic rheological tests. The shear viscosity behavior and shear stress of the bioinks (AP, APS@ (2:1, 9:1, 19:1)) were evaluated by applying shear rates ranging from 0.01 to 100 s^{-1}.

2.2.3. Fabrication of 3D printed APS@P scaffolds

The scaffolds were fabricated by extrusion 3D printer (BioScaffolder 3.1, GeSiM, Germany). The prepared bioinks (AP and APS@) were loaded into a printed tube and uniformly extruded layer-by-layer via a 22 G needle (diameter: 410 μm). The distance between each strand was set to 1 mm. The printing stress was fixed to 400 kPa, and the printing speeds of AP and APS@ bio-inks was 8 mm s^{-1}. All the scaffolds (AP and APS@) were printed with varying angle of 90° for adjacent layers (Table S3). The fabricated scaffolds were further cross-linked with 0.25 M EDC/NHS (Aladdin, China) in MES solution for 2 h (MES was dissolved in double-distilled water, and its pH was adjusted with NaOH to 6.5). Then, the scaffold was washed three times by distilled water to remove residual crosslinked regents. Subsequently, a 5 wt% ε-PL solution was employed to coat on the scaffolds' surface for 12 h. The resulting scaffolds was cleaned with double-distilled water to obtain the 3D printed APP and APS@P (2:1, 9:1, 19:1) scaffolds respectively. The scaffolds were recorded by a digital camera, and the porosity was analyzed according to the gross morphology images. Subsequently, the scaffolds were lyophilized.

2.3. Characterization of 3D printed APS@P scaffolds

2.3.1. Scanning electron microscope (SEM) imaging

A field emission scanning electron microscope (SEM, Hitachi S-4800, Japan) was employed to visualize the microscopic structure of the fabricated composite scaffold. Before SEM imaging, all samples were freeze-dried and then coated in platinum for 30 s (gold-plated observation).

2.3.2. Water contact angles test

The water contact angle of the APP and APS@P films were examined with an automatic video micro contact angle-measuring instrument. The deionized water falling on top surfaces of samples (n = 5) had a volume of 5 μL and a velocity of 1 $\mu L\ s^{-1}$, then images of droplets were recorded by microscope lens and a camera. Analysis and processing software was used to calculate the contact angle of the APP and APS@P.

2.3.3. Mechanical test

A compression test was conducted using a biomaterial testing system (INSTRON5967, INSTRON, USA). The compressive strain of the scaffolds with dimensions of 10 mm × 10 mm × 3 mm was assessed at a loading speed of 1 mm min^{-1}. The data was recorded automatically by the instrument and used for mechanical parameter calculation.

2.3.4. Degradation test of the bioink hydrogels

The weight loss of the bioink hydrogels immersed in phosphate buffered saline (PBS) was measured for degradation analysis. In short, the weight of the freeze-dried bioink hydrogels was set to W1, and sample was immersed and shaken in 20 mL PBS at 37 °C. Fresh PBS solution was changed every two days. At different intervals, the bioink hydrogels were removed and washed three times with double distilled water. After freeze-drying, the residual weight of the bioink hydrogels are recorded as W2. Degradation Weight lost (%) = (W1-W2)/W1 × 100 %.

2.3.5. Drug release assay

The APS@ and APS@P scaffolds with different ratio (2:1, 9:1, and 19:1) were immersed in PBS with gentle agitation, and the release of SAB was monitored at specified time intervals (12 h, 24 h, 3 days, 5 days, 7 days, and 10 days). The release profile was analyzed using high-performance liquid chromatography (HPLC, Agilent 1200, USA) with a Thermo C18 column (250 × 4.6 mm, 5 μm) at 25 °C. The mobile phase consisted of 0.1 % phosphoric acid and acetonitrile (780:220), with a flow rate of 1.8 mL/min. Sample injection volume was 10 μL with UV detection at 286 nm for analysis. Additionally, the SAB release from the APS@P (2:1) scaffold was monitored over an extended period (1 day, 3 days, 5 days, 7 days, 9 days, 12 days, 15 days, 20 days, 30 days, 40 days, 50 days, 60 days, and 70 days).

2.4. Bioactivity and bone-targeting property of APS@P composite 3D printing scaffold

2.4.1. Bone targeting validation assay

BTLs were fluorescently labeled with rhodamine B and incorporated into APP bio-ink hydrogels for composite scaffold fabrication. The composite scaffolds were immersed in double-distilled water with gentle shaking for 3 days at 4 °C. After incubation, the extract solution was collected for a hydroxyapatite affinity test. Hydroxyapatite powders were introduced into the collected scaffold extract solution and incubated for 3 h with gentle shaking. Subsequently, the hydroxyapatite powder was collected, washed three times with double-distilled water, and examined using a fluorescent microscope (ECLIPSE, Nikon, Japan) to verify whether the scaffold-released BTLs retained their ability to bind hydroxyapatite. Rhodamine B solution was used as a control.

2.4.2. Live and dead staining

The APS@P (2:1, 9:1, 19:1) scaffolds were applied to the bottom of a 12-well plate, and C3H10 cells (mouse cell line, C3H10-T1/2, ATCC, cat. CCL-226, Manassas, Virginia, USA) were seeded onto the scaffolds with 3×10^4 cells per well. After 48 h of culture, live/dead assay was performed using the CalceinAM/PI double staining kit (Abbkine, China). Imaging was captured by ultra-high-resolution confocal microscopy (SpinSR10, OLYMPUS, Japan), and live/dead cells were quantified using Image Pro Plus 6.0 software (Media Cybernetics, Inc., USA).

2.4.3. Cell viability assay

C3H10 cells were seeded in 96-well plates at a density of 5×10^3 cells per well. Cells were treated with the 3-day extract medium of APP and APS@P (2:1, 9:1, 19:1) scaffold. Cell viability (CCK-8, Dojindo, Kumamoto, Japan) was assessed after 48 h' incubation.

2.4.4. Cell attachment assessment

The printed scaffolds were placed on a PDMS film and seeded with 1×10^4 cells in 200 μL of culture medium for 3 h. After this incubation period, the scaffolds were removed, and the PDMS film along with the residual culture medium was transferred to a 24-well plate for CCK-8 testing. To each well, 100 μL of working solution (CCK-8:α-MEM = 1:9) (CCK-8, Dojindo, Kumamoto, Japan) was added. Following a 2-h incubation, the absorbance at 450 nm of 100 μL solution from each well was measured using a microplate spectrophotometer (Multiskan GO, Thermo Fisher, USA) and recorded as OD1. Additionally, OD2 was measured from 1×10^4 cells in 200 μL of culture medium. The cell attachment ratio was then calculated based on these measurements.

The printed scaffolds were placed on a PDMS film and seeded with 1×10^4 cells in 200 μL of culture medium for 3 h. After incubation, the scaffolds were removed, and the PDMS film along with the residual culture medium was transferred to a 24-well plate for CCK-8 testing. To each well, 100 μL of working solution (CCK-8:α-MEM = 1:9, Dojindo, Kumamoto, Japan) was added. Following a 2-h incubation, the absorbance at 450 nm of 100 μL solution from each well was measured using a microplate spectrophotometer (Multiskan GO, Thermo Fisher, USA) and recorded as OD1. Additionally, OD2 was measured from 1×10^4 cells in 200 μL of culture medium. The cell attachment ratio was then calculated based on these measurements.

$$\text{Cell attachment}(\%) = \frac{OD2 - OD1}{\text{OD2}} \times 100\% \quad (1)$$

2.4.5. DPPH free radical scavenging assay

The free radical scavenging activity of both SAB and SAB-BTL was evaluated using a DPPH free radical scavenging assay kit (Beijing Solarbio Science and Technology Co., Ltd., China). DPPH (1,1-diphenyl-2-picrylhydrazyl) is a stable nitrogen-based free radical, and its scavenging capacity can be assessed by measuring the reduction in absorbance, which reflects the compound's antioxidant potential. For the assay, samples of SAB and SAB-BTL (3 mg/mL, 100 μL) were mixed with the kit's working extraction solution (900 μL) and centrifuged at 10,000 rpm for 10 min. The resulting supernatant (25 μL) was then added to the kit's working solution (975 μL) and designated as the A1 solution. Another 25 μL of the same supernatant was added to anhydrous ethanol (975 μL) to prepare the A2 solution. As a control, the mixture of the kit's extraction solution and the working solution was used and labeled as A0. All solutions (A1, A2, and A0) were incubated in the dark at room temperature for 30 min. The absorbance was then measured at 515 nm using a spectrophotometer (Epoch, BioTek Instruments, USA), with ascorbic acid serving as a positive control for comparison. The DPPH free radical scavenging capacity (%) was calculated using the following formula:

$$\text{DPPH free radical scavenging capacity}\ (\%) = \frac{(\text{A0} - (\text{A1} - \text{A2}))}{\text{A0}} \times 100\% \quad (2)$$

Each sample was tested in triplicate, and the mean and standard deviation were calculated to ensure accuracy and reproducibility. This method effectively quantifies the antioxidant properties of SAB and SAB-BTL, allowing for the comparison of their free radical scavenging capabilities.

2.4.6. qRT-PCR assay

C3H10 cells and EA.hy926 cells (human cell line, ATCC, cat. CRL 2922, Manassas, Virginia, USA) were seeded on 6-well plates at a density of 1×10^5 cells per well. The 3-day extract medium of APP and APS@P (2:1, 9:1, 19:1) scaffold, along with SAB-BTL, were used to treat cells for 1–3 days. Total RNA was collected after 1 and 3 days of treatment. RT-PCR was conducted to evaluate the expression of osteogenic marker genes related to bone formation, including alkaline phosphatase (*Alp*), transcription factor 2 (*Runx2*), osteocalcin (*Ocn*), and osteoblast-specific transcription factor (*Osterix*). Additionally, angiogenesis genes such as vascular endothelial growth factor (*Vegf*), and angiopoietin (*Epo*) were also assessed. Gene primers were obtained from Sangon Biotech (Shanghai) Co., Ltd. China, with sequences provided in Table S4.

2.4.7. ALP staining experiment

C3H10 cells were seeded in 12-well plates at a density of 1×10^4 cells per well and cultured with the scaffold extract solution and SAB-BTL. After seven days of treatment, cells were washed with PBS and fixed with 4 % paraformaldehyde. The ALP staining commercial kit (Leagene Biotechnology, Beijing, China) was employed to assess the secretion of the osteogenic marker ALP according to the manufacturer's instructions.

2.4.8. Cell scratch migration assay

EA.hy926 cells were cultured in a 6-well plate at a density of 5×10^4 cells per well. A cell-free wound area was generated by gently scraping with a sterile pipette tip. The cells were then treated with the APS@P scaffold extract solutions and SAB-BTL for 3 days. Microscopy was employed to capture images after 12 h of treatment, and the migration width was documented using a microscope (ECLIPSE, Nikon, Japan) and quantified with Image Pro-Plus.

2.4.9. Transwell cell migration assay

APS@P scaffold extract solutions and SAB-BTL were introduced to the lower chamber of the Transwell plate, while C3H10 MSCs were seeded in the upper chamber at a density of 1×10^5 cells. Following 12-h and 24-h incubations, cells were stained with a 0.5 % crystal violet solution for 20–30 min. After careful removal of cells from the upper chamber, transwell migration cells were visualized using an optical microscope (ECLIPSE, Nikon, Japan).

2.4.10. Western blotting assay

MSCs lysates were prepared by homogenizing samples in radio immunoprecipitation assay (RIPA) buffer (P0013C, Beyotime, Shanghai, China) on ice. Proteins were isolated through centrifugation at 10,000×*g* for 10 min at 4 °C. The supernatant (30 μg of protein per sample) was subjected to SDS-PAGE and subsequently transferred to polyvinylidene fluoride (PVDF) membranes (FFP77, Beyotime, Shanghai, China). PVDF membranes were incubated overnight at 4 °C with primary antibodies: Tph2 (ab184505, Abcam, UK), β-catenin (ab32572, Abcam, UK), Alkaline Phosphatase (ALP) (R23427, ZenBioscience, China), Axin1 (2087S, Cell Signaling Technology, USA), all diluted at 1:1000. GAPDH (ab181602, Abcam, UK) was used as a loading control at a dilution of 1:5000. For secondary detection, membranes were treated with goat anti-rabbit IgG (A21020, Abbkine, USA) or Goat Anti-Rabbit lgG (L3012, Signalway Antibody, USA) at a dilution of 1:5000 for 1 h at 37 °C. Immunoreactive bands were visualized using a FluorChem® Q Imaging System (ProteinSimple, Santa Clara, CA, USA), and protein expression levels were quantified with Image J software, normalized to GAPDH.

2.4.11. RNA sequencing (RNA-Seq)

MSCs (C3H10) were treated with SAB (1 μM) for 24 h. Total RNA was isolated using the TRIzol reagent (Takara Bio Inc., Japan). The RNA samples were analyzed by the Beijing Genomics Institute (BGI), China. Specifically, the RNA samples were denatured to relax secondary structures, and mRNA was purified using oligo(dT)-attached magnetic beads. The purified mRNA underwent fragmentation at an optimal temperature. First-strand cDNA synthesis was performed, followed by second-strand cDNA synthesis to produce double-stranded cDNA. The double-stranded cDNA fragments were end-repaired, and an 'A' nucleotide was added to the 3′ ends of the blunt fragments. Adaptors were ligated to the cDNA fragments, and PCR amplification was performed to amplify the ligated products. The PCR products were denatured to yield single-stranded molecules, which were then circularized. Uncyclized linear DNA molecules were digested, and the circularized single-stranded DNA underwent rolling circle amplification to create DNA nanoballs (DNBs). The high-quality DNBs were loaded onto patterned nanoarrays using high-intensity DNA nanochip technology. Sequencing was performed using the combinatorial Probe-Anchor Synthesis (cPAS) method on the DNBSEQ platform (BGI). Data were processed and analyzed on the Dr. Tom II network platform provided by BGI (https://biosys.bgi.com/).

2.4.12. ELISA assay

MSCs were treated with 1 μM SAB for 72 h. The cell culture supernatant was then collected for a 5-HT ELISA test, using the ELISA kit (H104-1-1, Nanjing Jiancheng Bioengineering Institute, China) according to the manufacturer's instruction.

2.5. The effect of APS@P scaffold treatment on bone regeneration of ovariectomized osteoporotic bone defect

2.5.1. Animal study protocol

Thirty-two female aged 10-week SD rats were purchased from Beijing Vital River Laboratory Animal Technology Co., Ltd., China. The rats were randomly assigned to four groups (n = 8 per group) Rats were randomly assigned to different groups to evenly distribute potential confounding variables across all groups. The groups are: Control (femoral defect only), OBD model (OVX + femoral defect), OBD + APP (OVX + femoral defect treated with APP scaffold), and OBD + APS@P (OVX + femoral defect treated with APS@P (2:1) scaffold). Rats in the OBD, OBD + APP, and OBD + APS@P groups were anesthetized with 4 % isoflurane and 1 L/min oxygen and then underwent bilateral ovariectomy. One-week post-ovariectomy, 3 mm × 3 mm cylindrical bone defects were created in the lateral metaphysis of the distal femur using an electrical drill. APP and APS@P (2:1) 3D-printed scaffolds were implanted into the respective bone defects for 12 weeks' treatment.

All experimental procedures were conducted in strict accordance with the guidelines of the "Guide for the Care and Use of Laboratory Animals" issued by both the Guangdong Laboratory Animal Monitoring Institute and the National Laboratory Animal Monitoring Institute of China. These procedures were performed under protocols approved by the Specific Pathogen-Free animal care unit of the Animal Center at Zhanjiang Central Hospital, Guangdong Medical University, with Laboratory Animal Use Permit Number SYXK(粤)2023-0335. The Academic Committee on the Experimental Animal Ethics Committee of Zhanjiang Central Hospital, Zhanjiang, P.R. China, also approved these procedures under Permit Number ZJDY2023-01.

2.5.2. Micro CT analysis

After 12 weeks of treatment, all rats were euthanized, and their femurs were collected, fixed in 4 % paraformaldehyde, and prepared for micro-CT and histological analyses. Micro-CT analysis was conducted using a Viva CT40 scanner (Scanco, Switzerland) with the following parameters: 200 ms integration time, 70 kVp energy, 114 μA intensity, and 8 W power. The CT value was calibrated at 1200 mg HA/cm. The

region of interest (ROI) for bone defects was defined as a cylindrical volume with a diameter and height of 3 mm, centered on the defect for quantitative assessment. A threshold value of 70 was used to differentiate bone from soft tissue. For the proximal tibial metaphysis (PTM) analysis, the ROI extended 0–3 mm distal to the growth plate-epiphyseal junction, excluding cortical bone. Three-dimensional (3D) trabecular parameters (BV: bone volume; TV: tissue volume; BV/TV: bone volume/tissue volume; Tb.N: trabecular number; Tb.Th: trabecular thickness; Tb.Sp: trabecular separation; BS/BV: bone surface/bone volume; Conn.D: Connectivity density; BMD: Bone mineral density) were calculated, and 3D images were generated using the built-in Scanco software.

2.5.3. Histological analysis

The collect femur samples were performed decalcification in a 12 % EDTA solution for 1 month, followed by embedding in paraffin for histological sectioning. Hematoxylin and eosin (H&E) staining (Nanjing Jiancheng Bioengineering Institute, China) was performed and visualized in a microscope (ECLIPSE, Nikon, Japan).

2.5.4. Immunofluorescent analysis of osteogenesis, osteoclast activity, and osteogenic type H vessels

Immunofluorescent staining was utilized to analyze osteogenesis markers (OCN, RUNX2), osteoclast activity marker (RANKL), and osteogenic type H vessel markers (CD31 and Endomucin). Deparaffinized and rehydrated sample sections (5 μm) underwent immunofluorescence assays according to standard protocols. The sections were treated with proteinase K (50 μg/mL) for 20 min at 37 °C in a humidified chamber, followed by antigen retrieval. After antigen retrieval, samples were blocked with a buffer containing 5 % goat serum and 0.3 % Triton X-100 in PBS for 1 h at 37 °C. Subsequently, a double staining immunofluorescence assay was performed. Primary antibodies for OCN (1:100, 29697, Signalway Antibody, USA), Runx2 (1:100, ab76956, Abcam, UK), RANKL (1:100, 41789, Signalway Antibody, USA), CD31 (1:100, ab222783, Abcam, UK), and Endomucin (1:100, sc-65495, Santa cruz biotechnology, USA) were prepared in a diluent buffer. The sections were incubated with the primary antibodies overnight at 4 °C. After incubation, the sections were rinsed three times with PBS and then incubated with secondary antibodies: Alexa Fluor 488-conjugated (4412S, 1:200, Cell Signaling Technology, USA), or Alexa Fluor 555-conjugated (4409S, 1:200, Cell Signaling Technology, USA) at 37 °C for 1 h. Following this, the sections were rinsed with PBS and mounted with anti-fade medium containing DAPI (Yeasen Biotech, China) for nuclear staining. Fluorescence images were captured using a confocal ultrahigh-resolution microscope (SpinSR10, OLYMPUS, Japan). For each sample, at least six images were randomly taken from different locations within the defect area (20 × magnification) and used for analysis. The positive expression of OCN, RUNX2, RANKL, CD31, and Endomucin in the defect region was quantified using Image-Pro Plus 6.0 software (Media Cybernetics, USA) and presented as mean fluorescence density.

2.6. Statistical analysis

The data analysis utilized SPSS 19.0 statistical software. The Student's t-test is used to compare the means between two groups, whereas One-way ANOVA is used to compare the means among three or more groups. ANOVA with Fisher Least Significant Difference (LSD) was employed for statistical significance assessment under conditions of homogeneity of variances, while Tamhane's T2 (M) was applied for statistical significance evaluation in instances of heterogeneity of variance. A significance level of $P \leq 0.05$ was considered indicative of statistical significance.

3. Results and discussion

3.1. Preparation and characterization of SAB-BTL

Given the promising potential of SAB for OBD repair, its therapeutic effectiveness is limited by low bone-targeting efficacy and susceptibility to oxidation. In this study, we designed a liposome drug delivery system to enhance SAB's stability and further modified the liposomes with pyrophosphate-cholesterol to confer bone-targeting ability. Thus, the SAB-BTL was first formulated. Pyrophosphate-cholesterol served as the bone-targeting guide group for the liposomes due to its robust affinity for hydroxyapatite (the principal inorganic component of bone). The liposome formulation was employed with the reverse-phase evaporation method, a technique extensively elucidated in prior investigations [39,40]. Transmission electron microscopy (TEM) images demonstrated the two-dimensional image of SAB-BTLs, indicating a round shape with liposome bilayer outer membrane morphology (Fig. 2A). SAB-BTL exhibited uniform dispersion in PBS, forming a homogeneous solution with polydispersity index of 0.138 (Table S1). The encapsulation efficiency of SAB in the liposomes was determined to be 34.73 % by HPLC, featuring an average particle size of 100.90 nm (Fig. 2A, Figure S1 A) and zeta potential of −21.70 mV (Figure S1 B).

3.2. Physical and chemical properties of 3D printed APS@P scaffolds

To address the common challenge of "burst release" and ensure long-term release of drug that affect the performance of drug-loaded scaffolds, the APS@P scaffold with controllable and sustained drug release properties was established through the electrostatic encapsulation strategy. This strategy is carried out by using positively charged ε-polylysine to electrostatically encapsulate the APS@ scaffold, which is loaded with negatively charged SAB-BTL liposomes. This electrostatic encapsulation layer enhances the stability of the interaction between SAB-BTL and the scaffold. In our previous work, we demonstrated that the Alg/ε-PL scaffold exhibits a positively charged surface [42]. The negatively charged SAB-BTL liposomes were incorporated into the scaffold, which is not only a simple mixture, but also allows for binding between the positive and negative charge components. Additionally, the ε-PL coating, with its positive charge, forms a strong electrostatic interaction with APS@ scaffold, creating a stable electrostatic encapsulation layer on its surface. Consequently, the APS@P scaffold forms an "electric charge sandwich" structure, comprising Alg/ε-PL(positive)-Liposome(negative)-ε-PL(positive). This structure effectively encapsulates SAB through electrostatic interaction, offering strong support for SAB sustain release. Moreover, ε-PL was selected as the encapsulating material to avoid introducing additional components.

Previous investigations demonstrated potent osteogenic effects of SAB at a concentration of 1 μM [27,43]. Consequently, the APS@ (9:1) bioink ratio was initially established, with the SAB concentration set at 1 μM. From this baseline, we established two additional APS@ ratios: 2:1 and 19:1. The 19:1 ratio corresponds to a 0.5 μM SAB dose, while the 2:1 ratio represents a 10 μM SAB dose. These three ratios (2:1, 9:1, and 19:1) were chosen to explore high, medium, and low SAB concentrations in order to identify the optimal ratio for scaffold fabrication. Oscillatory rheological analysis was then employed to examine the impact of SAB-BTL on the printing properties of the APS@ bioinks. With an increase in shear rate, the viscosity of all APS@ bioinks significantly decreased, revealing the shear-thinning nature essential for 3D printing. As the SAB-BTL content increases in the APS@ bioink, viscosity concurrently increases. The results demonstrate that SAB-BTL have no negative influence on printability of APS@ bioinks (Figure S2 A). FTIR spectra analysis showed that the incorporation of different ratio of SAB-BTLs did not result in the formation of any new chemical groups, indicating that no chemical reaction occurred between SAB-BTL and the Alg/ε-PL bioink (Figure S2 B). APS@ scaffold was fabricated as follows: the APS@ scaffold was 3D printed using APS@ bioinks

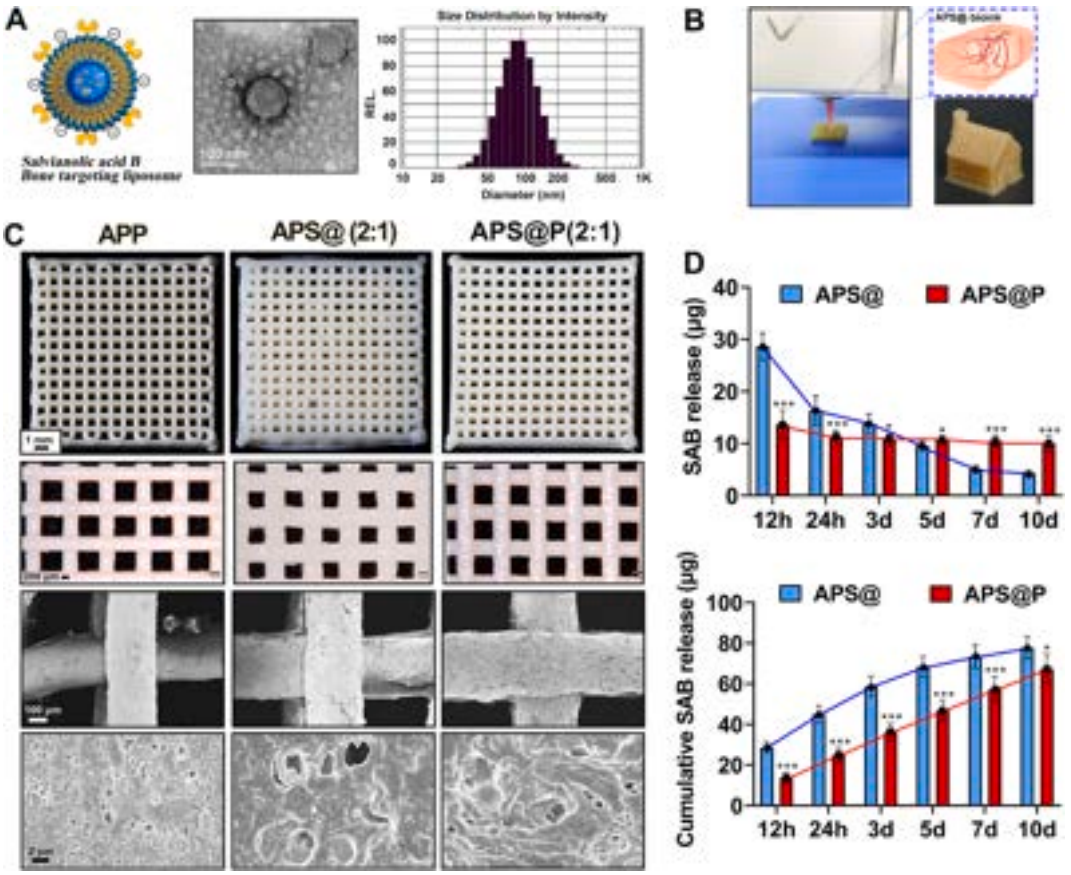

Fig. 2. Physical property characterization of SAB-BTL and SAB-BTL incorporated alginate/ε-polylysine scaffold (APS@ and APS@P). **A)** Transmission electron microscopy (TEM) images depict SAB-BTL liposomes, accompanied by a size distribution profile based on intensity; **B)** A 3D-printed scaffold produced using APS@ bioink prior to crosslinking is shown, highlighting the bioink's stability during the 3D printing process; **C)** Gross observations and scanning electron microscopy (SEM) images illustrate the morphological differences among APS@P, APS@(2:1), and APS@P (2:1) 3D printed scaffolds; **D)** A comparative analysis of SAB drug release profiles from the APS@ and APS@P scaffolds over a 10-day period is presented; Statistical significance was defined as $^{*}P < 0.05$, $^{**}P < 0.01$, $^{***}P < 0.001$. Number of replicates n = 6.

Note: Alginate/ε-polylysine 1:1 bioink is referred to as AP bioink; Alginate/ε-polylysine 1:1(ε-polylysine) scaffold is referred to as APP scaffold; SAB-BTL incorporated alginate/ε-polylysine 1:1 scaffold is referred to as APS@ scaffold; SAB-BTL incorporated alginate/ε-polylysine 1:1(ε-polylysine) scaffold is referred to as APS@P scaffold.

(alginate/ε-polylysine + SAB-BTL). Next, the printed APS@ scaffold was crosslinked with EDC/NHS. To further enhance the stability of SAB-BTL loading and scaffold fabrication, we recoated the APS@ scaffold with ε-polylysine, resulting in the APS@P scaffold. This additional processing step significantly strengthens the connection between SAB-BTL and the scaffold, ensuring a robust and stable integration. Fig. 2B demonstrates the 3D printing process using APS@ bioink (before crosslinking). The printed house model suggests that APS@ bioink exhibits excellent stability and 3D printing characteristics. The gross morphology images of different ratios of APS@ and APS@P scaffolds (2:1, 9:1, and 19:1) are shown in Fig. S3. Macroscopic morphology and scanning electron microscopy (SEM) revealed that the APS@P scaffold possessed high fidelity and a regular porous structure, with an average pore size of 547 ± 14 μm and filament diameter of 500 ± 13 μm. The surface of APP scaffold appeared smooth, while the introduction of SAB-BTLs increased surface roughness in APS@P scaffold (Fig. 2C). The enhanced roughness may provide a conducive environment for cell attachment.

To determine whether our APS@P scaffold could overcome the "burst release" issue commonly associated with drug-loaded scaffolds, we performed drug release characterizations and monitored them over 10 days by high-performance liquid chromatography (HPLC). The APS@P scaffold was immersed in PBS for testing. Compared to the APS@ scaffold, which lacked ε-polylysine recoating, the APS@P scaffold exhibited a consistently linear, near-zero-order release kinetics of SAB. This characteristic prevented the "burst" release and ensured a nearly constant release rate over 10 days (Fig. 2D). Conversely, the APS@ scaffold showed a significant burst release of SAB on the first day, followed by a gradual decrease over time. The drug release profile of SAB from APS@P scaffolds was monitored over 80 days. The cumulative release exhibited a consistent linear increase, with over 60 % of the loaded SAB released by day 80 (Figure S4A). As shown in Figure S4B, a comparison of SAB release profiles for different ratios of APS@ and APS@P scaffolds (2:1, 9:1, and 19:1) over 10 days demonstrates that the various ratios of APS@P scaffolds maintain a consistent and stable release pattern. In contrast, SAB release from the APS@ scaffolds was much faster and significantly higher than from the APS@P scaffolds. Additionally, while drug release from the APS@ scaffolds decreased significantly over time, the APS@P scaffolds exhibited stable and sustained release, with no marked decline. These results highlight the effectiveness of the electrostatic encapsulation strategy in improving the stability and control of drug release in APS@P scaffolds. Although AP bioinks and SAB-BTLs have a basic electrostatic interaction facilitating SAB-BTL binding, this alone does not ensure stable release. The addition of ε-polylysine electrostatic encapsulation layer acts as a "shell", thus contributing not only to maintaining scaffold stability but also enabling a stable and constant release of SAB. This electrostatic encapsulation of SAB-BTL with non-covalent binding is advantageous for the controlled release of SAB during the degradation of the APS@P scaffold in a

physiological environment.

Degradation experiment results revealed APP and APS@ bioinks exhibited approximately 20 % weight degradation after 60 days in PBS shaking, indicating a stable physical behavior (Fig. S5). In addition, there was no significant difference in water contact angle of the APS@P and the APP films, indicating that the incorporation of SAB-BTL do not affect the hydrophilicity of the scaffold (Fig. S6). Fig. S7 demonstrates that SAB-BTL had a minimal effect on the porosity of the APP scaffolds. However, the compression modulus and strength of APS@P scaffolds decreased significantly with increasing SAB-BTL content (Fig. S8). This reduction is attributed to SAB-BTL's inhibition of the electrostatic interactions and crosslinking between Alg and ε-PL.

3.3. In vitro evaluation of 3D printed APS@P scaffold

3.3.1. Cell viability, compatibility, and targeted properties of APS@P scaffold

To assess the cell compatibility and viability of the APS@P scaffold, mesenchymal stem cells (MSCs, C3H10 cell line) were employed in the initial test. MSCs were seeded on the APS@P (2:1, 9:1, and 19:1) and APP hydrogels for 48 h, following evaluation with live/dead assay. Qualitative and semi-quantitative results of live/dead staining demonstrated that both of APP and APS@P (2:1, 9:1 and 19:1) groups exhibited high cell survival rates after 48 h of incubation. APS@P (9:1) scaffold demonstrated a significantly higher MSCs' survival rate compared to APP scaffold. In general, the 48-h cell survival rate of APP and APS@P scaffold group all reached more than 85 %, which affirms the high biocompatibility of APP and APS@P (2:1, 9:1, 19:1) scaffolds. After seeded MSCs on the APP, APS@P (2:1, 9:1, and 19:1) hydrogels and

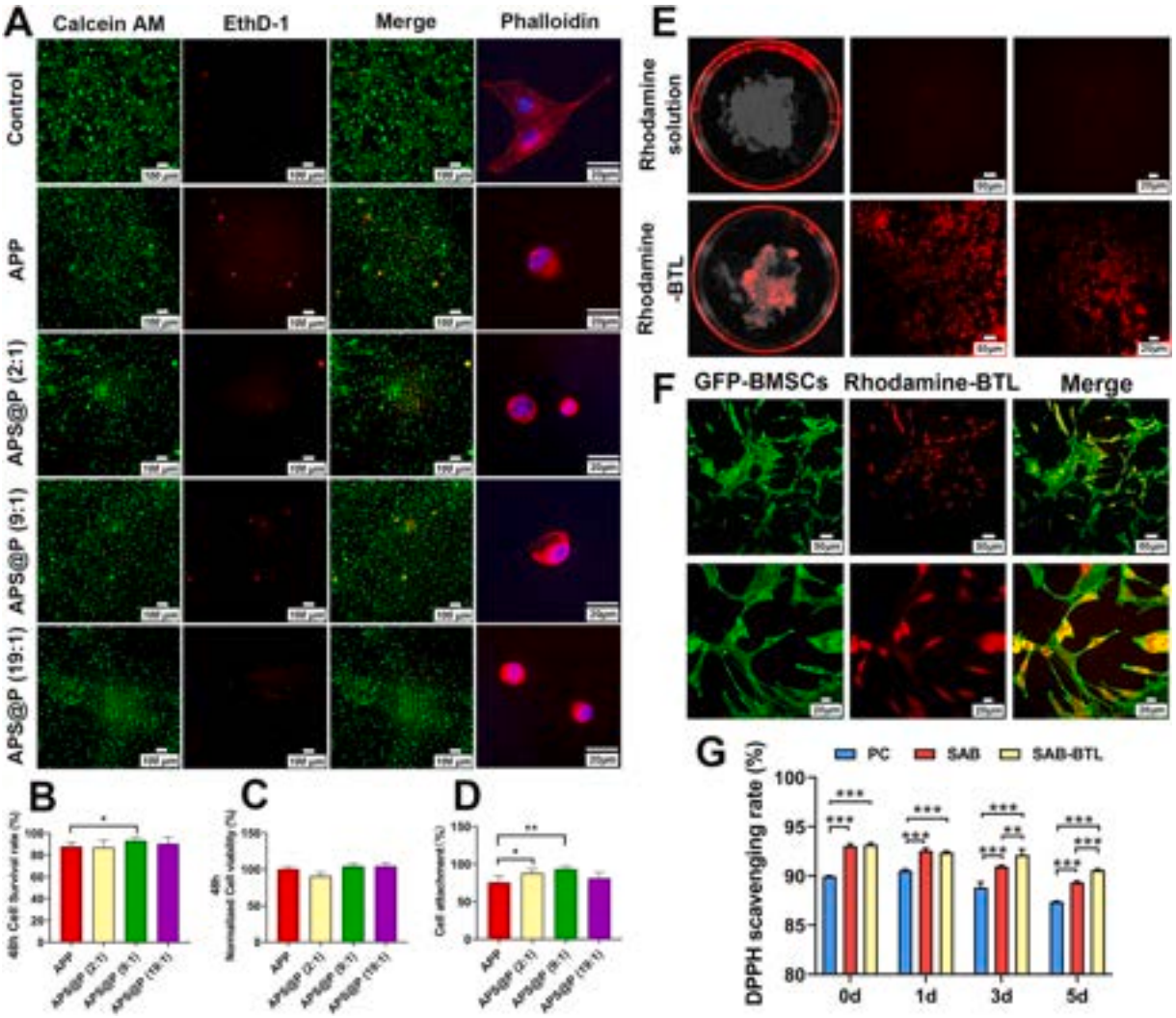

Fig. 3. Characterization of APS@P Scaffolds and SAB-BTL: Cytotoxicity, cell viability, attachment, internalization, hydroxyapatite affinity test, and DPPH scavenging assays of SAB/SAB-BTL. **A)** Representative live-dead images of MSCs (C3H10 cell) cultured on APS@P (2:1, 9:1, and 19:1) and APP scaffolds for 48 h. Live cells are marked in green, while dead cells are indicated in red. Additionally, cytoskeletal (pink) and nuclear (blue) staining images of MSCs cultured on these scaffolds after 48 h are provided. **B)** Semi-quantitative analysis of live-dead assay results. **C)** CCK-8 cell viability assay of MSCs (C3H10 cells) cultured with extract medium from APP and APS@P (2:1, 9:1, and 19:1) composite scaffolds for 48 h. **D)** Percentage of MSCs' attachment on 3D-printed scaffolds (APP, APS@P 2:1, 9:1, and 19:1) after 3 h of culture. **E)** Hydroxyapatite affinity assay: Representative images depict the results of the hydroxyapatite affinity test using rhodamine B-labeled BTL-incorporated APP 3D composite scaffolds. Scaffold extracts were incubated with hydroxyapatite for 6 h at different magnifications. Free rhodamine B solution served as the control. **F)** Cell internalization: Representative images of cell endocytosis assay using rhodamine B-labeled bone-targeting liposome incorporated APP 3D composite scaffolds incubated with MSCs for 24 h. Green indicates MSC cytoskeleton staining, red indicates internalized rhodamine B-labeled liposomes. **G)** Antioxidant activity: Evaluation of SAB and SAB-BTL antioxidant capacity using the DPPH (2,2-Diphenyl-1-picrylhydrazyl) free radical scavenging assay. Vitamin C was used as positive control (PC). Statistical significance was defined as $^{*}P < 0.05$, $^{**}P < 0.01$, and $^{***}P < 0.001$. Number of replicates n = 6.

cultured for 48 h, MSCs exhibited distinct cell morphology, appearing rounder and smaller compared to the control, as depicted in cytoskeleton and nucleus staining images. This suggests that the APP and APS@P hydrogels moderately affected the extension and spread of the seeded MSCs' cytoskeleton within the initial stage of cultivation (Fig. 3A&B).

To further evaluate the compatibility and potential toxicity of the APS@P scaffold, we immersed APS@P 3D-printed scaffolds (ratios of 2:1, 9:1, and 19:1) in stem cell culture medium with agitation at 4 °C for 3 days. The 3-day extracts from these scaffolds were then used for cell viability tests using the CCK-8 viability kit, with extracts from the APP scaffold serving as a control. The CCK-8 viability results indicated that MSCs thrived and proliferated well in the APS@P scaffold extract medium incubated for 48 h, with no significant toxic effects observed, confirming its superior biocompatibility (Fig. 3C). A cell attachment assay was performed using the CCK-8 kit by measuring the optical density (OD) values for MSCs attached to a cell slide. The results demonstrated that cell attachment on the APS@P (2:1 and 9:1) scaffolds was significantly higher than on the APP scaffold (Fig. 3D). This suggests that the enhanced roughness of the APS@P scaffold may provide a more conducive environment for cell attachment compared to the APP scaffold.

The charge of nanoparticles, determined by various surface chemicals, plays a pivotal role in influencing bioactivity, circulation time, and interaction with resident macrophages within organs containing the mononuclear phagocyte system (MPS) [44]. Positively charged particles tend to accumulate more readily in the lungs, liver, and spleen. Conversely, neutral and negatively charged nanoparticles exhibit prolonged circulation time and reduced accumulation in the aforementioned MPS organs [45]. SAB-BTL with a negative charge has the potential to extend retention time, ensuring sufficient time for targeted delivery to the bone, if it is released from APS@P scaffold. In our previous study, cholesterol-pyrophosphate facilitated the targeted concentration of liposomes in fractured bones, significantly increasing drug retention time at the fracture site to over 20 days. It shows a high affinity to both corticoid bone and trabecular bone. Therefore, pyrophosphate-cholestrol used as a bone-targeting group for drug delivery has been proven to be effective [39,40].

An essential question is whether the BTL can be released from the APS@P scaffold while maintaining its bone-targeting ability. This was investigated by conducting hydroxyapatite affinity tests using the extract medium from the APS@P scaffold after PBS incubation. Hydroxyapatite, a primary component of the skeleton, was used as the bone-targeting substrate for *in vitro* testing [46]. Rhodamine B was used to fluorescently label the BTL. After 24 h of incubation with hydroxyapatite, the rhodamine B-labeled BTLs exhibited a strong affinity for hydroxyapatite, displaying bright fluorescent binding. In contrast, the rhodamine B fluorescent solution used as a control showed little affinity for hydroxyapatite. This result indirectly verified that the SAB-BTL released from the APS@P scaffold maintains excellent bone-targeting capabilities and may effectively target bone tissue. (Fig. 3E). The bone-targeting property of the SAB-BTL is consistent with our previous studies [39,40]. The bone-targeting group "cholesterol-pyrophosphate" has a strong affinity for hydroxyapatite, similar to bisphosphonates due to its phosphate groups. However, unlike bisphosphonates, pyrophosphate is a naturally occurring substance in the human body and does not cause the potential side effects commonly associated with bisphosphonates [47]. To confirm whether SAB-BTL released from the composite scaffold could be internalized by cells, rhodamine B-labeled BTL were incorporated into APS@P scaffold and the extract medium of the scaffold was used to incubate MSCs for 24 h. Fluorescence images revealed that the released rhodamine B-labeled BTL were successfully internalized and enriched in MSCs (Fig. 3F).

Encapsulating SAB in liposomes is hypothesized to mitigate its oxidation process. To validate the antioxidant properties of both SAB and SAB-BTL, we conducted a 5-day DPPH (1,1-diphenyl-2-picrylhydrazyl) radical scavenging assay. The results indicate that both SAB and SAB-BTL (with an equivalent amount of SAB) exhibited similar DPPH scavenging rates after 1 day. However, after 3 days, SAB-BTL demonstrated a significantly higher DPPH scavenging rate compared to SAB, with this significant difference persisting even after 5 days. These findings reveal that the liposome formulation notably attenuates the oxidation of SAB. (Fig. 3G).

3.3.2. Stimulation of MSCs and endothelial cells (ECs) migration and ALP secretion by APS@P scaffolds

Delayed bone defect healing in osteoporotic patients is associated, in part, with decreased proliferation and migration of repair cells. To evaluate the effect of the scaffold on the migration of repair cells, scratch assays were employed to assess the impact of the APS@P scaffold extract solution on EC migration. Fig. 4A illustrates SAB-BTL group and APS@P (2:1, 9:1, 19:1) groups all promoted cell migration after 12 h of treatment, compared to the normal control group. The APS@P (2:1) group exhibited the most significant effect compared to the normal control and the APP group. Specifically, the ECs' migration of APS@P (2:1) group significantly increased 148 % more than the normal control and increased 78 % more than the APP group. Non-SAB loaded APP scaffold demonstrated no significant stimulation on the migration of ECs.

Transwell assays were subsequently conducted to further assess the impact of APS@P scaffold extract solutions on MSC migration. As shown in Fig. 4B, following a 12-h exposure to APS@P scaffold extracts and SAB-BTL, only the SAB-BTL group significantly promoted MSC migration. The other scaffold treatment groups did not demonstrate significant stimulation in cell migration compared to the normal control group. However, following 24 h of treatment exposure, the SAB-BTL group, APP group, and APS@P (2:1, 9:1, 19:1) groups all demonstrated a substantial increase in cell migration, with a minimum 219 % increase more than the normal control group. Particularly noteworthy is the APS@P (2:1) group, which exhibited a 383 % significant increase in cell migration more than the normal control and 51 % more than the APP group ($P < 0.001$). The migration assay results suggest that APS@P groups enhanced the migration of the repair cells (MSCs and ECs), especially, APS@P (2:1) group demonstrated the most pronounced effect on promoting migration of repair cells.

In a 7-day treatment of MSCs with the extract of the APS@P scaffolds, ALP staining results revealed that in comparison to the normal control group, the SAB-BTL group, APP group, and APS@P (2:1, 9:1, 19:1) groups exhibited a substantial increase with the APS@P (2:1) group showing the highest level (Fig. 4C). Especially, APS@P (2:1) increased ALP up to 333 % more than the normal control. Furthermore, when compared to the APP group, the APS@P (2:1, 9:1) groups displayed varying degrees of a significant increase, with the APS@P (2:1) group demonstrating the most pronounced stimulating effect on ALP secretion. GFP-labeled rBMSCs were seeded onto APP and APS@P (2:1, 9:1, 19:1) scaffolds and cultured for 7 days. ALP immunofluorescent staining was then performed to evaluate osteogenic ALP secretion from the rBMSCs. The results indicated that both APP and APS@P scaffolds promoted ALP secretion and stimulated osteogenic differentiation of rBMSCs. Notably, APS@P scaffolds showed greater stimulation of ALP secretion compared to APP, with APS@P (2:1) with APS@P (2:1) exhibiting the most concentrated ALP secretion. The ALP immunofluorescent staining of GFP-rBMSCs loaded APP and APS@P (2:1, 9:1, 19:1) scaffold culture for 7 days demonstrated similar results (Fig. S9).

3.3.3. Stimulation of osteogenic and angiogenic gene expression by APS@P scaffolds

Inadequate bone regeneration in osteoporotic bone injuries is associated with diminished osteogenic capability, enhanced osteoclastic absorption, and impaired bone vascularization [48]. An ideal scaffold for treating OBD should possess osteogenic and vascularization bioactivities [49]. To investigate the influence of BTL on the bioactivities of SAB, the osteogenic effects of SAB-BTL were first assessed in MSCs. The RT-PCR assays illustrate that SAB and SAB-BTL significantly stimulated

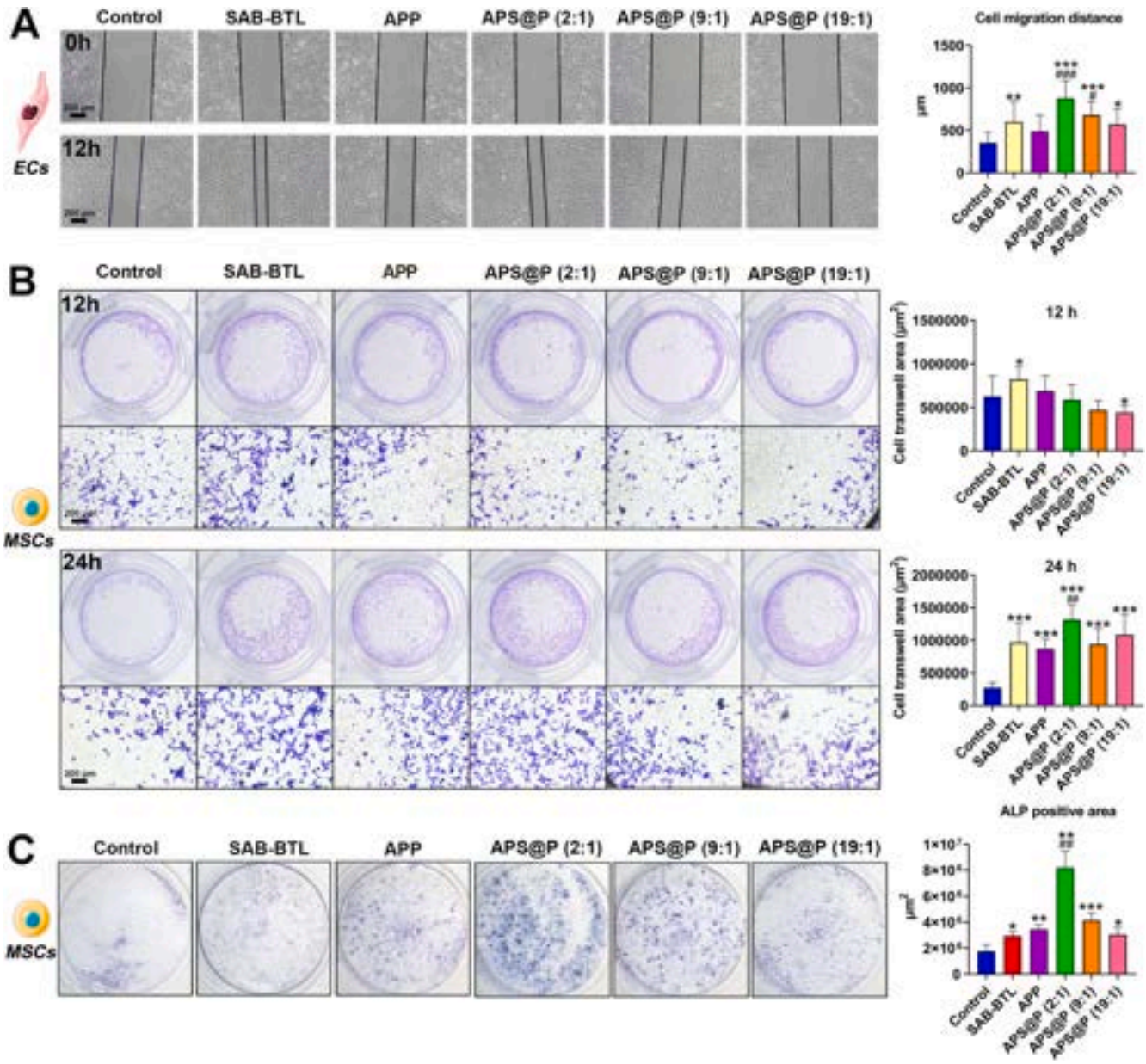

Fig. 4. *In vitro* migration stimulation of MSCs (C3H10) and ECs (EA.hy926) by scaffold extract medium (APP, APS@P (2:1, 9:1, 19:1)), and evaluation of osteogenic ALP activity. **A)** ECs Migration: Representative images and quantitative analyses of EA.hy926 cell migration treated with extract medium from composite scaffolds (APP, APS@P (2:1, 9:1, 19:1)) in a scratch wound healing assay, assessed at 0 and 12 h; **B)** MSCs Migration: Representative images and quantitative analyses of MSCs migration treated with extract medium from composite scaffolds (APP, APS@P (2:1, 9:1, 19:1)) in a transwell migration assay, assessed at 12 and 24 h; **C)** ALP Activity: Representative ALP stain images of MSCs cultured with SAB-BTL and extract medium from composite scaffolds (APP, APS@P (2:1, 9:1, 19:1)) after 7 days. ALP stain images were used to quantitative assessment of the osteogenic effect of the treatments. The extract medium from the APP and APS@P scaffolds (at ratios of 2:1, 9:1, and 19:1) were obtained by incubating the scaffolds in normal cell culture medium for three days. Statistical significance was defined as $^{*}P < 0.05$, and $^{**}P < 0.01$, $^{***}P < 0.001$ *vs* control group; $^{\#}P < 0.05$, and $^{\#\#}P < 0.01$, $^{\#\#\#}P < 0.001$ *vs* APP group. Number of replicates n = 6.

the osteogenic gene expression of *Ocn*, *Osterix*, *Runx2*, and *Alp* in MSCs after 1 day and 3 days of incubation compared to the normal control group (Fig. 5A). No significant difference emerged between the two treatment groups (SAB and SAB-BTL) at the 1days. Whereas, SAB-BTL exhibited the highest osteogenic gene expression among three groups. Notably, SAB-BTL significantly increased *Alp* (33 %), *Ocn* (35 %), *Osterix* (73 %), and *Runx2* (35 %) gene expression more than the treatment with the SAB solution alone after 3 days of incubation, respectively. These results imply that modification of BTL did not weaken the osteogenic promotion ability of SAB. Conversely, as time extended, SAB-BTL showed higher promotion of osteogenic ability than SAB. The results from cell internalization and DPPH assays provide direct evidence that a BTL delivery system can protect SAB against oxidation, improve its efficacy, and enhance its uptake into MSCs. These combined effects enable SAB-BTL to significantly increase the expression of osteogenic genes compared to the SAB solution.

To validate the osteogenic activity of APS@P scaffold with SAB-BTL loaded, the APP and APS@P (2:1, 9:1, 19:1) scaffold extract solutions were used to treat MSCs. MSCs play a crucial role in the recruitment, proliferation, and differentiation of bone repair cells in the fracture healing process [50,51]. RT-PCR results demonstrated that the extracts of APP and APS@P (2:1, 9:1, 19:1) scaffold all significantly increased the expression of *Ocn* and *Osterix* genes in MSCs compared to the normal control group after 1 day and 7 days Notably, APS@P groups showed

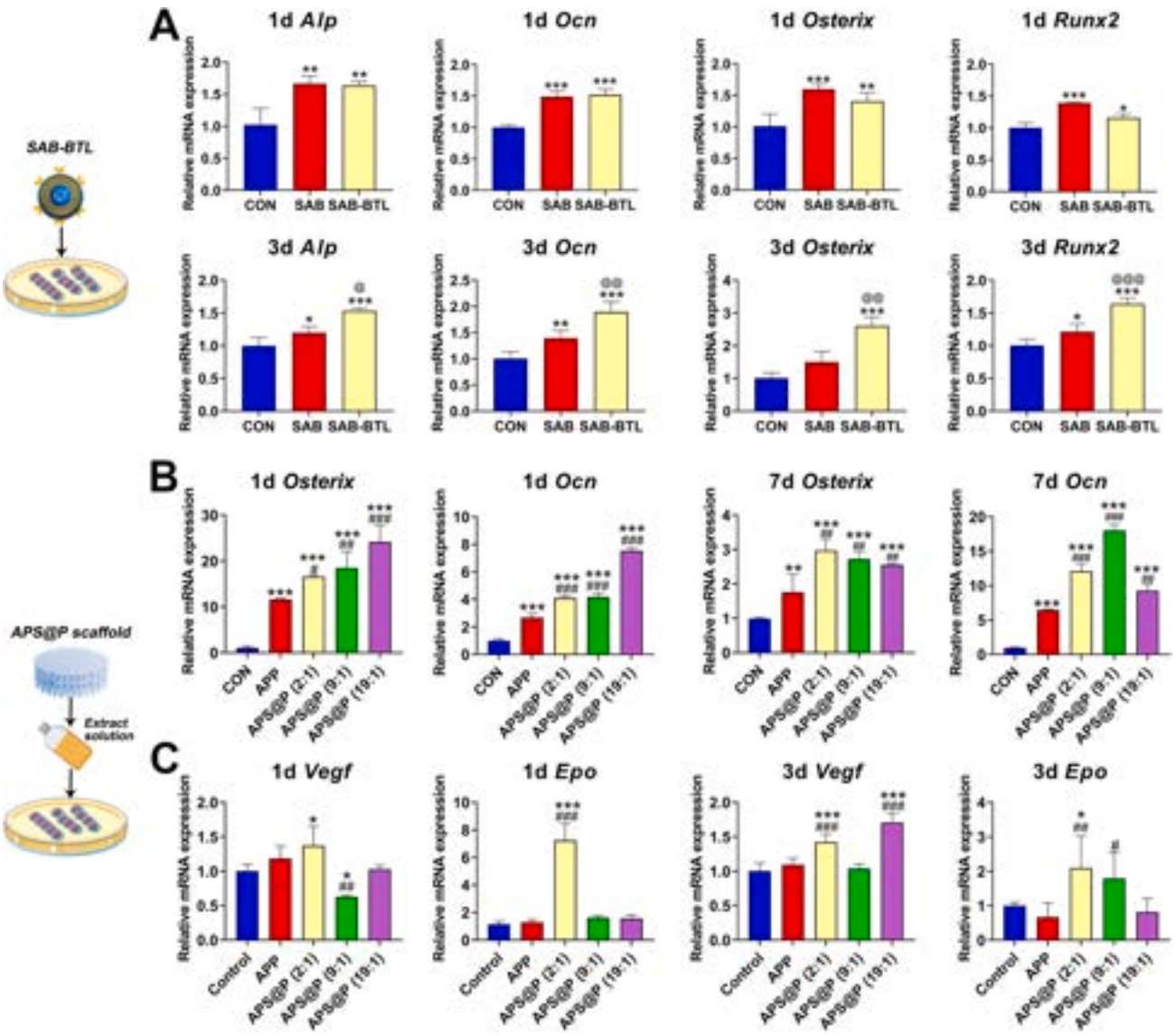

Fig. 5. Promotion of osteogenic differentiation of MSCs (C3H10) and angiogenesis of endothelial cells (EA.hy926) *in vitro* by SAB-BTL and extract medium of the composite scaffolds (APP, APS@P (2:1, 9:1, 19:1)). A) Impact of SAB and SAB-BTL on osteogenic biomarkers (*Alp*, *Ocn*, *Osterix*, and *Runx2*) of MSCs: RT-PCR quantified analysis quantified osteogenic biomarkers in MSCs treated with SAB-BTL for 1 day and 3 days; B) Impact of APS@P on osteogenic biomarkers of MSCs(*Ocn*, *Osterix*): RT-PCR analysis quantified osteogenic biomarkers in MSCs treated with extract medium from composite scaffolds (APP, APS@P at ratios of 2:1, 9:1, and 19:1) for 1 and 7 days; C) Impact of APS@P on angiogenesis biomarkers(*Vegf*, *Epo*) of ECs: RT-PCR analysis quantified angiogenesis biomarker in EA.hy926 cells treated with extract medium from composite scaffolds (APP, APS@P at ratios of 2:1, 9:1, and 19:1) for 24 h and 3 days. The extract medium from the APP and APS@P scaffolds (at ratios of 2:1, 9:1, and 19:1) were obtained by incubating the scaffolds in normal cell culture medium for three days. Statistical significance was defined as $^{*}P < 0.05$, $^{**}P < 0.01$, $^{***}P < 0.001$ *vs* Control, $^{\#}P < 0.05$, $^{\#\#}P < 0.01$, $^{\#\#\#}P < 0.001$ *vs* APP scaffold. Number of replicates n = 6.

significantly higher osteogenic gene expression compared to the APP group. Particularly, the APS@P (19:1) group demonstrated the most significant enhancement, showcasing an impressive 648 % increase in *Ocn* and a 1815 % increase in *Osterix* more than the normal control group at 1 day. Moreover, the elevation in *Ocn* and *Osterix* also significantly higher compared to the APP group. In addition, after 7 days, the APS@P (2:1) significantly increased *Osterix* expression by up to 201 % compared to the normal control and a 68 % increase compared to the APP group. The APS@P (9:1) showed a substantial enhancement, with an impressive rise in *Ocn* expression compared to both the normal control and the APP group. The results suggest that the APP scaffold can promote the osteogenic differentiation of MSCs, and loading with SAB-BTL into the APP scaffold can significantly enhance its osteogenic activity (Fig. 5B).

Successful bone repair and remodeling depend on sufficient blood supply and vascular reconstruction within the injured area [13,52,53]. EA.hy926 cells, a human hybrid endothelial cell line, were employed to evaluate the influence of the APS@P scaffolds on angiogenesis. To confirm the scaffold's angiogenic bioactivity, the expression of angiogenic biomarkers (*Vegf* and *Epo*) was evaluated in EA.hy926 cells after treatment with extract solutions from the APP and APS@P scaffolds. As shown in Fig. 5C, after 1 day and 3 days of exposure to the extracts, the APS@P (2:1) group exhibited a significant increase in the expression of *Vegf* and *Epo* genes compared to the normal control group, while APP group demonstrated no significant stimulation effects on angiogenesis. Particularly noteworthy is that the APS@P (2:1) group induced a remarkable 456 % and 214 % elevation of *Epo* gene expression at 24 h and 3 days, respectively, compared to the APP group. Since APP scaffold shows no significant effects on angiogenesis, the angiogenesis effects of APS@P should be attributed to SAB's function. Our previous study

demonstrated that SAB significantly increases angiogenesis and improves microcirculation in bone marrow [24]. Numerous studies have suggested that SAB serves as an effective anabolic agent for angiogenesis and is frequently incorporated into biomaterials [28,54,55], Specifically, some studies highlight that SAB primarily regulates the VEGF signaling pathway [56]. Additionally, SAB promotes angiogenesis and inhibits apoptosis by regulating autophagy [57]. SAB is a major component of *Salvia miltiorrhiza*, which has been traditionally used in China for the treatment of cardiovascular diseases. Previous studies indicate that the angiogenic effects of *Salvia miltiorrhiza* are associated with the inhibition of the miR-155-5p/HIF-1α/VEGF axis in acute myocardial infarction [58]. Furthermore, it has been shown to promote angiogenesis and treat myocardial ischemia through the Ang-1/Tie-2/FAK pathway [59]. In summary, SAB plays a crucial role in enhancing angiogenesis and microcirculation. Its mechanisms of action may relate to the regulation of VEGF and autophagy-associated signals.

The bone healing process involves sequential stages: initial repair cell migration and recruitment, subsequent vasculature formation, and finally bone formation [60]. *In vitro* findings indicate that APS@P scaffolds enhance the expression of both osteogenic and angiogenic genes in MSCs. Notably, APS@P (2:1) demonstrates superior efficacy in stimulating cell migration, ALP secretion, and gene expression related to angiogenesis compared to other ratios and the APP group. While APS@P (9:1) shows better performance in promoting osteogenic gene expression than APS@P (2:1), the latter provides a more comprehensive overall effect, making it the most suitable formulation for *in vivo* studies aimed at promoting healing of bone defects.

3.4. In vivo animal evaluation of the APS@P scaffold treatment

3.4.1. Ovariectomy (OVX) increased rat body weight

OVX serves as a widely accepted gold standard model for evaluating

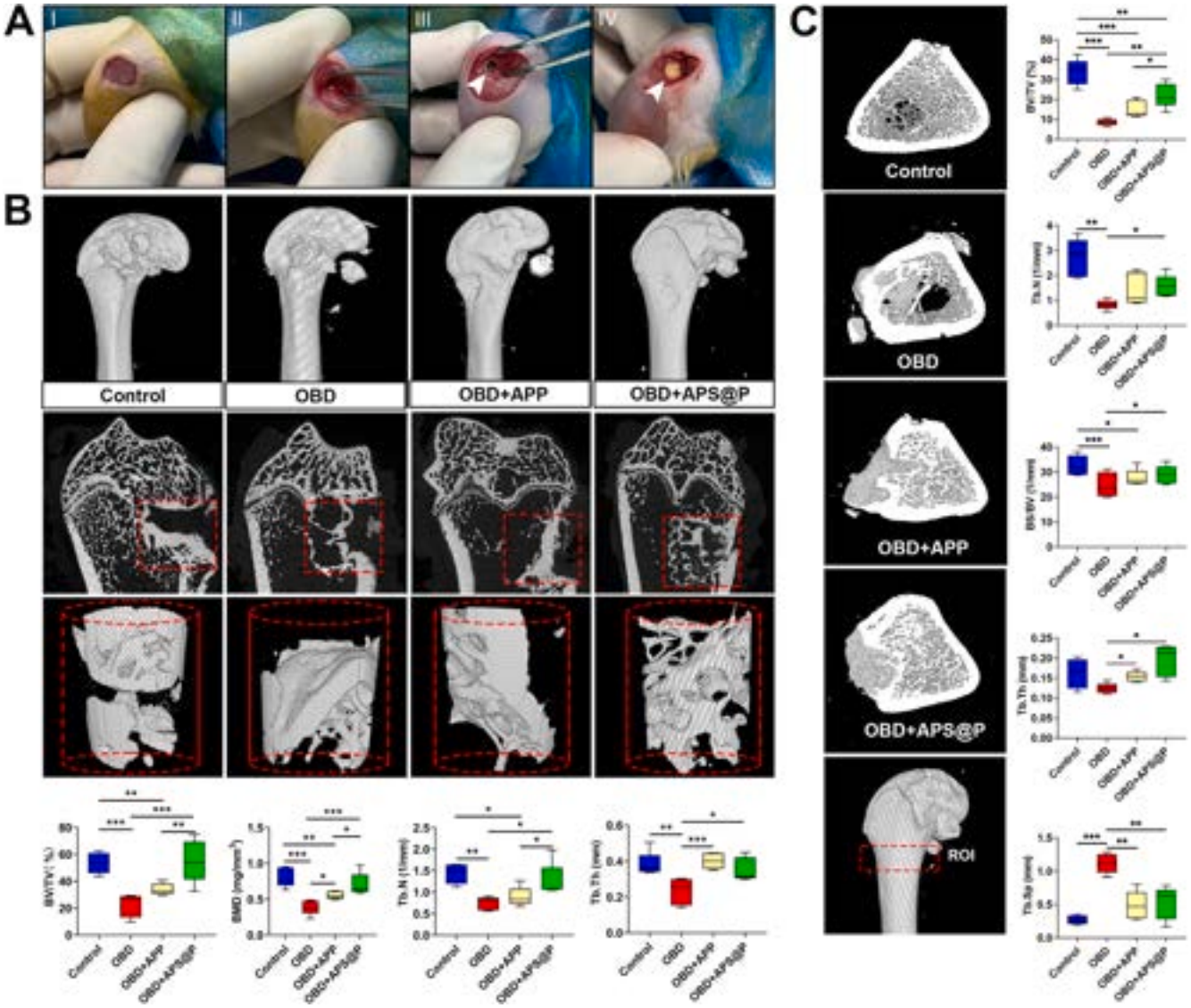

Fig. 6. Enhanced repair of critical bone defects in OBD rats by APS@P Scaffold. **A)** Surgical Procedure: Representative images illustrate the implantation of the APS@P scaffold for the treatment of OBD. **B)** Bone Regeneration Assessment: Representative 3D reconstructed images of bone defects, accompanied by quantitative micro CT analysis, demonstrate significant bone regeneration after 12 weeks of APS@P scaffold treatment in OBD rats. **C)** Trabecular Bone Analysis: Representative 3D reconstructed images and corresponding quantitative micro CT analysis of trabecular bone in the femoral metaphysis, evaluated after 12 weeks of APS@P scaffold treatment. This region of interest (ROI) analyzed is located beneath the scaffold implantation site to assess bone regeneration beyond the immediate scaffold area. BV: bone volume; TV: tissue volume; BV/TV: bone volume/tissue volume; Tb.N: trabecular number; Tb.Th: trabecular thickness; Tb.Sp: trabecular separation; BS/BV: bone surface/bone volume; Conn.D: Connectivity density; BMD: Bone mineral density. Statistical significance was defined as $^{*}P < 0.05$, $^{**}P < 0.0$, and $^{***}P < 0.001$. Number of samples n = 6.

the preventive and therapeutic effects of drugs on postmenopausal osteoporosis [61]. In this study, bilateral OVX was performed to establish a rat model of postmenopausal osteoporosis. As depicted in Fig. S10, by the 12th-week endpoint, the body weight of all OBD rats was significantly higher than that of the normal rats with bone defect control group. The weight gain observed in OVX rats indirectly indicated the successful establishment of the OVX rat model [62] as estrogen decline due to OVX can induce weight gain. Scaffold implantation treatment was initiated concurrently with the bone defect creation surgery, except for the normal defect control group and the OBD model group (Fig. 6A). The *in vivo* experiment was conducted over 12 weeks.

3.4.2. Stimulation of bone regeneration in bone defect of OVX rats by APS@P scaffold treatment

The bone regeneration capacity of the APS@P scaffold was assessed in an OBD rat model, with normal rat bone defect models serving as controls (Fig. 6B). Micro-CT imaging of the rat femoral region revealed significantly impaired healing in the OBD regions compared to the normal bone defect controls. Longitudinal 2D micro-CT images indicated limited bone repair within the defect site and along its margins in OBD rats, with minimal cortical bone regeneration. OVX-induced osteoporosis led to a 58 % reduction in bone volume/tissue volume (BV/TV), a 52 % decrease in bone mineral density (BMD), a 39 % reduction in trabecular thickness (Tb.Th), and a 48 % decrease in trabecular number (Tb.N) within the bone defect area. Additionally, there was a significant 28 % decrease in bone surface/bone volume (BS/BV), an 85 % reduction in bone connectivity density (Conn.D), and a 178 % increase in trabecular separation (Tb.Sp) (Fig. S11) compared to the normal bone defect group ($P < 0.05$). In comparison, treatment with the APP scaffold in OBD rats demonstrated enhanced bone regeneration along the cortical bone margins. This resulted in a 46 % increase in BMD, a 72 % increase in Tb.Th, and a 46 % reduction in Tb.Sp in the bone defect ($P < 0.05$). While BV/TV, Tb.N, Conn.D, and BS/BV showed slight increases, these changes were not statistically significant. On the other hand, the APS@P (2:1) scaffold exhibited a more pronounced effect on bone regeneration in the OBD model. This treatment increased BV/TV by 146 %, Tb.N by 70 %, and Tb.Th by 51 %. There was also a substantial 466 % increase in Conn.D, an 87 % increase in BMD, a 23 % increase in BS/BV, and a 36 % reduction in Tb.Sp compared to the untreated OBD group ($P < 0.05$).

Notably, the APS@P (2:1) scaffold outperformed the APP scaffold, with the APS@P group showing a 62 % increase in BV/TV, a 42 % increase in Tb.N, a 28 % increase in BMD, and a 112 % improvement in Conn.D ($P < 0.05$) compared to the APP group. No significant differences in Tb.Sp, Tb.Th, or BS/BV were observed between the APS@P and APP groups.

These findings highlight the superior efficacy of the APS@P (2:1) scaffold in promoting bone regeneration and improving bone microstructure in OBD, offering significant improvements over both untreated and APP scaffold-treated models (Fig. 6B & Fig. S11).

3.4.3. Stimulation of trabecular formation in distal femur metaphysis of OVX rats by APS@P scaffold treatment

Similar trends were observed in the distal femur metaphysis below the defect site (Fig. 6C). Micro-CT analysis revealed substantial decreases in key bone parameters in the OBD group compared to the normal control group. Specifically, there was a significant 74 % reduction in BV/TV, a 66 % reduction in Tb.N, a 25 % decrease in BS/BV, and a 78 % drop in Conn.D, accompanied by a significant 270 % increase in Tb.Sp ($P < 0.05$). These results indicate significant bone loss and trabecular microstructure degradation, confirming the successful establishment of the OVX osteoporosis model. After 12 weeks of treatment, the APP scaffold resulted in a 75 % increase in trabecular BV/TV, a 78 % increase in Tb.N, and a 14 % increase in BS/BV in the metaphyseal region of the distal femur. However, these changes did not reach statistical significance compared to the OBD group. The APP scaffold did, however, induce a significant 18 % increase in Tb.Th and a 45 % decrease in Tb.Sp compared to the OBD group ($P < 0.05$).

In contrast, the APS@P(2:1) scaffold demonstrated more pronounced and statistically significant improvements. There was a significant 153 % increase in BV/TV, along with an 18 % increase in BS/BV, a 31 % increase in Tb.Th, an 87 % rise in Tb.N, a 144 % increase in Conn.D, and a 40 % decrease in Tb.Sp compared to the OBD group ($P < 0.05$). These results underscore the superior therapeutic efficacy of the APS@P(2:1) scaffold in promoting bone mass and improving bone microstructure. Additionally, APS@P(2:1) treatment led to a significant 45 % increase in BV/TV compared to the APP group ($P < 0.05$), highlighting its enhanced osteogenic effects.

The APS@P(2:1) scaffold facilitated substantial new bone formation within the defect region and accelerated the healing of adjacent bone, promoting better osteointegration between the scaffold and host bone. This improved integration may enhance bone strength, increase scaffold stability, and reduce the risk of secondary fractures. For critical-sized defects, materials must provide both mechanical support and promote osteogenesis. In osteoporotic conditions, the APS@P scaffold not only offers stable mechanical support through osteoconduction, but also delivers additional osteogenic and bone-targeting benefits. Therefore, the APS@P scaffold was specifically designed to address the unique challenges of OBD.

3.4.4. APS@P scaffold treatment suppress RANKL, stimulates OCN and RUNX2 expression, and promotes type H vessel formation on OBD rats

Histological analyses, including H&E staining and immunofluorescent staining, were conducted to assess the healing of OBDs (Fig. 7). H&E staining revealed that the cortical bone defects were primarily filled with fibrous tissue without significant callus formation in the control and OVX defect groups. The APP scaffold showed moderate enhancement in bone formation, with limited small bone formations observed within the scaffold. In contrast, APS@P(2:1) resulted in substantial new bone formation within the defect areas, with numerous trabecular bones filling the adjacent bone area (Fig. 7A).

RANKL immunofluorescent staining was carried out to evaluate the impact of the scaffolds on osteoclast activity *in vivo* (Fig. 7B). The results indicated a significant increase in RANKL expression in trabecular bone following OVX compared to the control. Importantly, the APP scaffold induced a more pronounced elevation compared to the OVX defect groups. In contrast, the APS@P(2:1) scaffold significantly reduced RANKL expression compared to the APP group. These findings suggest that APP scaffold implantation may enhance RANKL-mediated osteoclastogenesis, while incorporating SAB-BTL could mitigate the increased osteoclastogenesis induced by OVX and scaffold implantation. Similar results were observed outside the implanted scaffold (Fig. S12). The OBD model, OBD + APP, and OBD + APS@P treatment groups all showed significantly higher RANKL protein expression compared to the normal defect control, whereas APS@P treatment suppressed RANKL protein expression compared to APP treatment. Therefore, APS@P(2:1) scaffold treatment may mitigate excessive bone resorption, enhancing osseointegration by inhibiting osteoclastogenesis. Our previous study demonstrated that salvianolate significantly suppress osteoclast activity by regulating RANKL/OPG signaling cascade. SAB, as a principal ingredient in salvianolate, also demonstrated significant inhibition of RANKL activity, consistent with our previous findings [29].

OCN and RUNX2 double immunofluorescent staining were also performed to assess ostegenesis in bone defect sections (Fig. 7C). The results revealed that OVX significantly suppressed the expression of osteogenic biomarkers, including a significant decrease in OCN and RUNX2. Notably, both the APP and APS@P(2:1) scaffold treatments significantly stimulated the protein expression of OCN and RUNX2 compared to the OBD group. Specifically, the APS@P(2:1) scaffold induced a more pronounced osteogenic response increase in OCN and RUNX2 compared to the APP scaffold group. The highest levels of OCN and RUNX2 staining were observed in the APS@P(2:1) group,

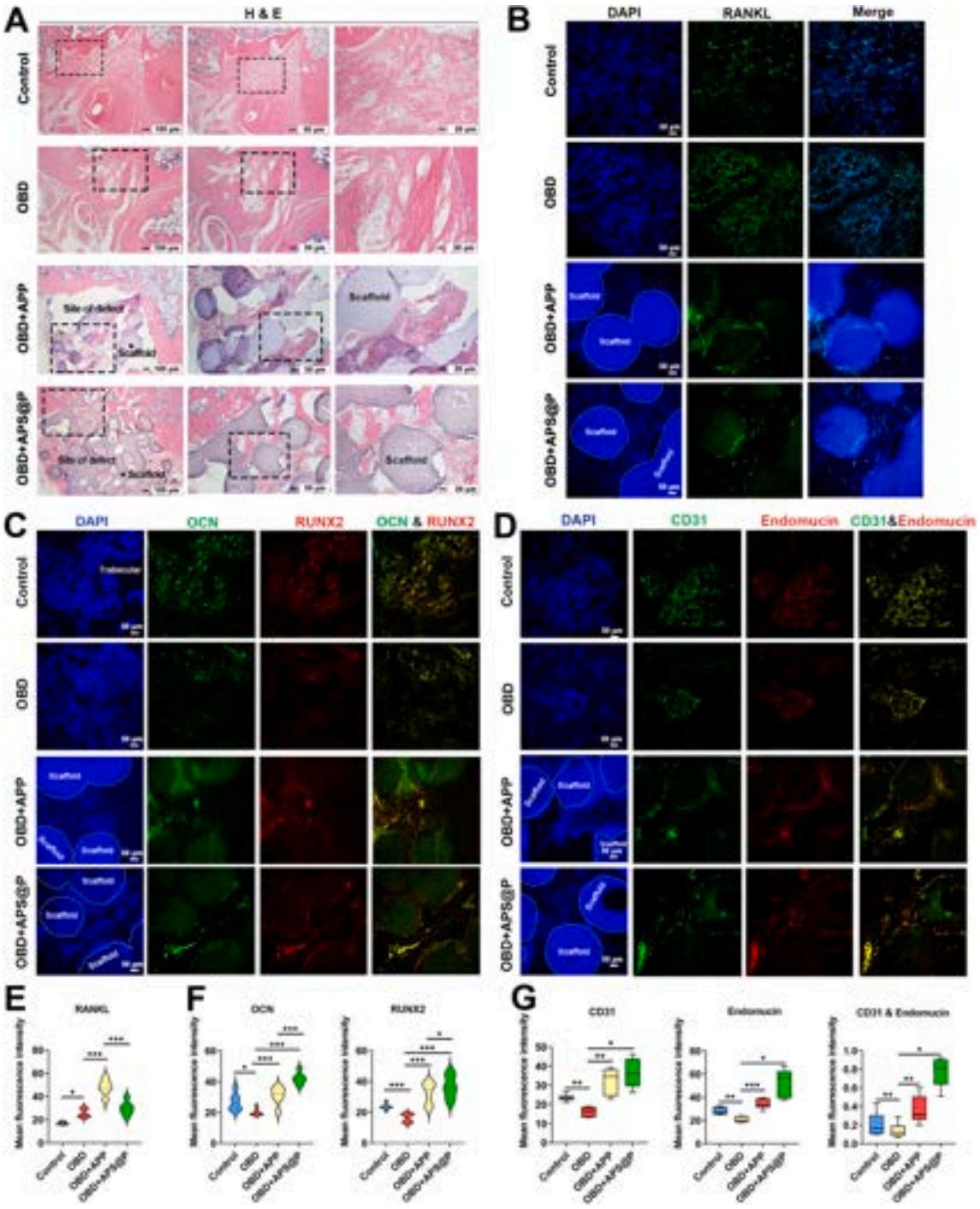

Fig. 7. Histological and immunofluorescence analysis of bone defect regeneration in OBD rats treated with APS@P scaffold. **A)** Representative images of H&E staining depicting the defect area across different treatment groups; **B)** Representative immunofluorescence staining images showing RANKL expression in each group, with green fluorescence indicating RANKL-positive expression; **C)** Representative immunofluorescence staining images demonstrating OCN and RUNX2 expression in each group, where green fluorescence indicates OCN-positive expression and red fluorescence indicates Runx2-positive expression; **D)** Representative immunofluorescence staining images illustrating CD31 and Endomucin expression in each group, with green fluorescence indicating CD31-positive expression and red fluorescence indicating Endomucin-positive expression. Yellow fluorescence indicates overlap of CD31 and Endomucin, highlighting the presence of osteogenic type H vessels. **E)** Quantitative analysis of RANKL expression by immunofluorescence is provided for each group; **F)** Quantitative analysis of OCN and RUNX2 protein expression by immunofluorescence is provided for each group; **G)** Quantitative analysis of CD31, Endomucin, and CD31 & Endomucin overlap expression by immunofluorescence across groups. Statistical significance was defined as $^{*}P < 0.05$, $^{**}P < 0.01$, and $^{***}P < 0.001$ indicates statistical significance. Number of samples n = 6.

suggesting that APP and SAB-BTL exerted synergistic effects for promoting new bone regeneration. Similar results were observed outside the implanted scaffold (Fig. S13). OBD model group significantly decreased OCN and RUNX2 expression compared to the normal defect control group. The OBD + APP and OBD + APS@P treatment groups all showed significantly higher OCN and RUNX2 protein expression compared to the OBD model group.

Type H vessels, a subtype of capillaries intricately linked to

osteogenesis, play a crucial role in regulating new bone formation [63]. These vessels orchestrate bone formation by generating factors that stimulate the proliferation and differentiation of osteoprogenitors within the bone marrow. These vessels feature a concentrated population of osteoprogenitors, predominantly expressing Osterix, facilitating osteoprogenitors' differentiation into osteoblasts and osteocytes. A comprehensive understanding of the spatiotemporal regulation of angiogenesis is essential. Equally important is understanding the interaction between tissue-engineered structures and the host vascular microenvironment. To evaluate osteogenic type H vessel formation among groups, CD31 and Endomucin immunofluorescent double staining were performed on the bone defect slices (Fig. 7D). The results revealed that OBD significantly suppressed the expression of angiogenesis biomarkers, leading to a significant decrease in CD31 and Endomucin. Additionally, OBD significantly inhibited the overlap expression of CD31 & Endomucin compared to the normal bone defect control, indicating a strong inhibition of type H vessel formation. Both APP and APS@P(2:1) scaffold treatments significantly stimulated the expression of CD31, Endomucin, and CD31 & Endomucin overlap expression compared to the OBD group. Especially, APS@P(2:1) impressively promoted CD31 & Endomucin overlap expression by 451 % more than the OBD group. APS@P(2:1) scaffold inducing a more beneficial effect on angiogenesis of CD31 and Endomucin expression compared to the APP group.

Type H vessels, densely surrounded by osteoprogenitors expressing the transcription factor Osterix, highly expressed after APS@P(2:1) scaffold treatments. The result was align well with the *in vitro* data, APS@P extracts treatment induced 648 % rise in *Ocn* and 1815 % surge in *Osterix* gene expression of MSCs more than the normal control. OBD model group significantly decreased CD31 and Endomucin expression compared to the normal defect control group. The OBD + APP and OBD + APS@P treatment groups all showed significantly higher CD31 and Endomucin protein expression compared to the OBD model group. While a prior investigation suggested that the osteoporotic phenotype does not influence the angiogenic response during the reparative healing stage [64], we posit that osteoporosis may not significantly affect the overall angiogenic response. However, it could selectively inhibit the formation of osteogenic-coupled type H vessels during the healing process. And APS@P(2:1) treatment effectively mitigates the OVX-induced impairment of osteogenic type H vessels and promotes the proximity of osteoprogenitors to these vessels, establishing a source of osteoblasts crucial for bone formation. The *in vivo* results indicated high drug efficacy within the APS@P(2:1) scaffold system. Consequently, cells within the bone defect received continuous, abundant, and consistent stimulation to promote bone healing. Similar results were observed outside the implanted scaffold (Figs. S13–S15). The scaffold's sustained local release of SAB not only upregulated the activities of OCN and RUNX2, thereby enhancing MSCs' osteogenic differentiation and promoting the formation of osteogenic type H vessels, but also suppressed RANKL-mediated osteoclastogenesis (Fig. 7E-G). This APS@P(2:1) system effectively regulates multiple signaling pathways simultaneously to address osteoporotic defects, demonstrating superiority over current clinical treatments.

Salvia miltiorrhiza, a traditional Chinese medicine commonly used for treating cardiovascular and cerebrovascular diseases, contains an active polyphenol component known as SAB. SAB has shown significant potential in promoting bone formation by enhancing osteoblast differentiation and stimulating angiogenesis [24,25,28,54]. Our study not only supports these findings but also highlights SAB's critical role in enhancing the osteogenic differentiation and migration of MSCs. Additionally, our research demonstrates SAB's capacity to stimulate endothelial cell migration and promote the formation of type H vessels, further contributing to bone regeneration.

3.5. The osteogenic potential mechanism of SAB in bone healing associated with stimulating the Tph2/Wnt/β-catenin signaling pathway

The significant efficacy of APS@P in repairing OBD in rats prompted our investigation into its underlying mechanisms. SAB, an essential osteogenic agent incorporated into the APS@P scaffold, underscores the importance of understanding its functional mechanism. In this study, we used RNA-Seq analysis to investigate the effects of SAB treatment on MSCs. Gene set enrichment analysis (GSEA) revealed significant alterations in the folate biosynthesis pathway following SAB treatment (Fig. 8A). Further analysis showed a marked upregulation of the *Alpl* gene, a key marker of osteogenic differentiation. This increase in *Alpl* expression confirms that SAB promotes osteogenesis in MSCs, as ALP is a well-known biomarker of bone formation. Our subsequent investigations further focus on elucidating the mechanisms by which SAB induces osteogenesis in MSCs.

Significantly, the RNA-Seq heat map revealed that SAB treatment notably upregulated the expression of the *Tph2* gene (Fig. 8B), which encodes the rate-limiting enzyme in serotonin (5-hydroxytryptamine, 5-HT) biosynthesis. Previous studies demonstrated that *Tph2* knockout mice ($Tph2^{-/-}$) exhibit significantly reduced bone mass, affecting both axial (vertebrae) and long bones. Mice with partial *Tph2* knockdown ($Tph2^{+/-}$) showed a significant reduction in osteoblast numbers and bone formation rate, along with increased osteoclast surface and bone resorption markers [65]. This evidence highlights the critical role of *Tph2* in bone metabolism, where it not only promotes osteoblast generation and bone formation but also inhibits osteoclast activity.

Building on this, we confirmed via RNA-Seq, RT-PCR, and Western blot analyses that SAB stimulates *Tph2* gene and protein expression (Fig. 8C&D&E). *Tph2* regulates 5-HT biosynthesis, which, although primarily known as a neurotransmitter, has also been implicated in bone metabolism [66]. Our ELISA analysis further demonstrated a significant increase in 5-HT levels in the culture medium of SAB-treated MSCs (Fig. 8F). Previous research has shown that 5-HT can activate the Wnt/β-catenin signaling pathway, which is crucial for osteogenesis by regulating osteoblast proliferation and differentiation. This pathway also interacts with other signaling networks such as BMP, TGF-β, FGF, Hippo, Hedgehog, Notch, and PDGF to regulate bone metabolism [67]. Specifically, previous studies revealed that 5-HT promotes the translocation of Axin1 and enhances its interaction with 5-HT receptors (Htr1b/1d/1f). Axin1 is a critical component of the β-catenin degradation complex, which inhibits Wnt/β-catenin signaling. By binding to Htr1b/1d/1f, Axin1 is prevented from forming this complex, thereby stabilizing β-catenin. The β-catenin can then accumulate, translocate into the nucleus, and activate Wnt signaling pathways [68]. Our results are consistent with these findings, demonstrating that SAB treatment significantly increases Tph2 expression and 5-HT production, which in turn enhances β-catenin expression. SAB treatment also suppressed the expression of Axin1 and APC (both involved in β-catenin degradation, negative regulate factor of Wnt signaling), further stabilizing β-catenin and activating downstream Wnt signaling. These findings support the conclusion that SAB stimulates the Tph2—5-HT—Wnt/β-catenin signaling axis in MSCs, amplifying the osteogenic signal cascade. While multiple studies have reported SAB's ability to enhance stem cell differentiation through Wnt signaling [24,32,69,70], our study is the first to demonstrate the upstream molecular events connecting SAB to Wnt/β-catenin signaling via the promotion of *Tph2* and 5-HT expression.

Furthermore, beyond the osteogenic effects of SAB, previous research has shown that SAB mitigates microcirculation disturbances in glucocorticoid-induced osteoporosis (GIO) rats [24]. Consistent with these findings, we observed similar microcirculation disturbances in OBD rats, particularly a deficiency of type H vessels. Notably, the APS@P scaffold significantly enhanced the formation of osteogenic type H vessels in these rats. Type H vessels are closely linked to increased osteogenic differentiation of MSCs, which leads to the generation of more osteoprogenitor cells. Coupled with APS@P's stimulation of EC

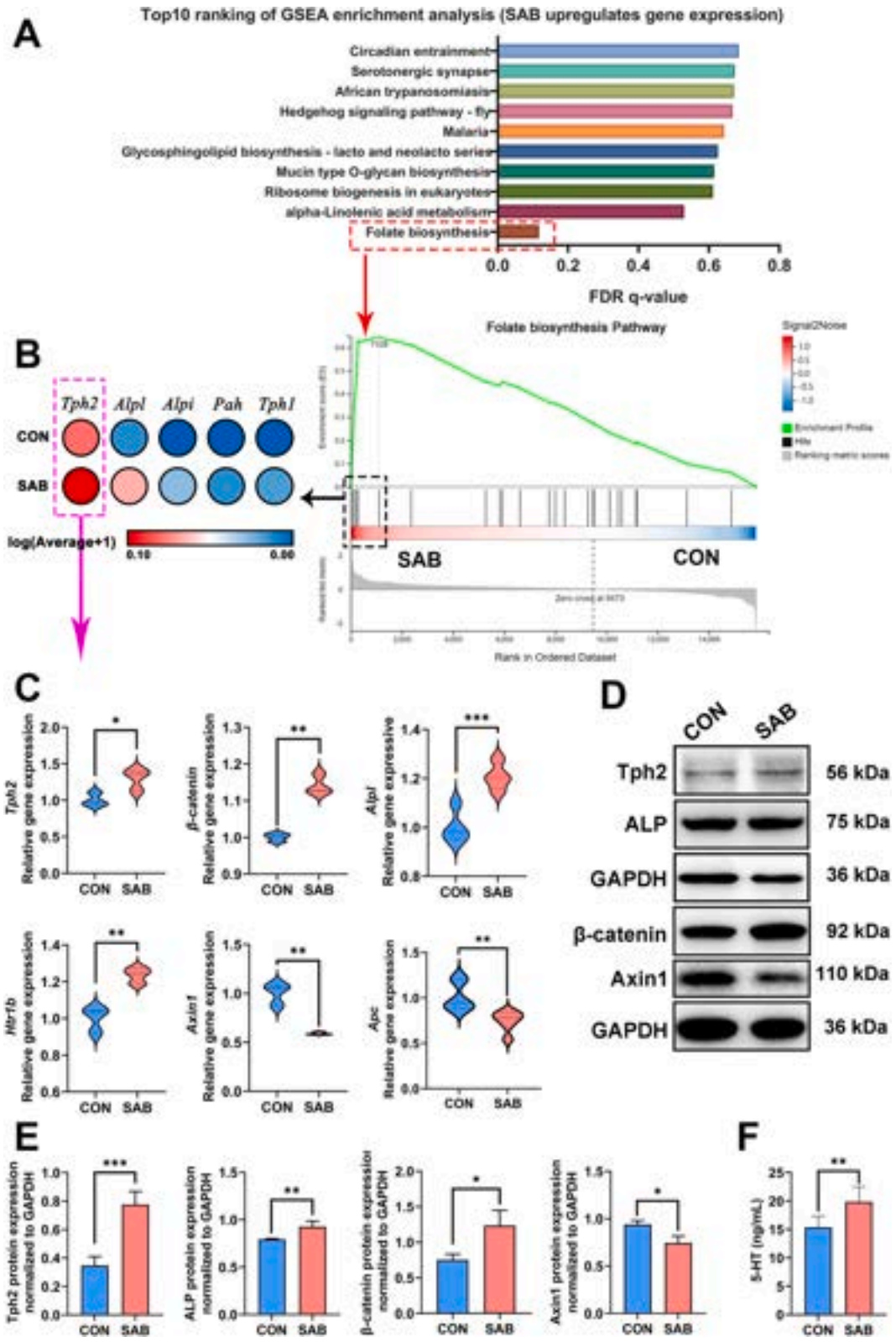

Fig. 8. Transcriptome sequencing analysis (RNA-Seq) of the SAB treatment on MSCs: upregulation and molecular biological validation. **A)** Gene Set Enrichment Analysis (GSEA) of the effects of SAB treatment on MSCs; **B)** Enrichment map of genes involved in the folate biosynthesis pathway and heat map showing upregulation of genes in SAB-Treated MSCs; **C)** qRT-PCR validation of upregulated genes *Tph2* and *Alpl*, and their associated genes involve in Tph2/Wnt/β-catenin signaling pathways. **D)** Western Blot validation of protein expressions of Tph2, ALP, Axin1, and β-catenin in MSCs. Number of replicates n = 3. **E)** Quantitative analysis of Western Blot protein expression of Tph2, ALP, Axin1, and β-catenin. **F)** ELISA analysis of serotonin (5-HT) in the culture medium supernatant of SAB-treated MSCs. Statistical significance was defined as $^{*}P < 0.05$, $^{**}P < 0.01$, and $^{***}P < 0.001$ indicates statistical significance. Number of replicates n = 6.

angiogenesis and migration, this process promotes the formation of type H vessels, thus improving the osteogenic nutritional microenvironment. Additionally, APS@P suppresses RANKL-induced osteoclastogenesis in OBD rats. This finding aligns with previous research, which demonstrated that salvianolate (with SAB as the main bioactive component) regulates the RANKL/OPG signaling pathway, inhibiting RA-induced bone loss by reducing RANKL secretion from osteoblasts [29]. RANKL production is primarily driven by osteoblasts and bone marrow stromal cells, with osteoblasts playing a critical role in maintaining the RANKL/OPG balance, a key determinant of osteoclast differentiation. By promoting osteogenesis, APS@P enhances osteoblast generation. The sustained release of SAB from APS@P scaffolds also reduces osteoblast-mediated RANKL production, thereby inhibiting RANKL-driven bone resorption.

This evidence suggests that SAB exerts a dual effect: it not only promotes osteoblast activity but also inhibits osteoclastogenesis by downregulating RANKL expression. This dual modulation of bone formation and resorption is particularly significant in OBD repair, where both promoting new bone formation and inhibiting bone loss are critical.

In summary, we propose that the underlying mechanism of APS@P in OBD involves promoting the osteogenic differentiation of MSCs by activating the Tph2/Wnt/β-catenin signaling axis, coupled with the stimulation of type H angiogenesis and suppression of RANKL-mediated bone resorption. Together, these processes help establish a microenvironment that restores bone homeostasis and enhances regeneration in

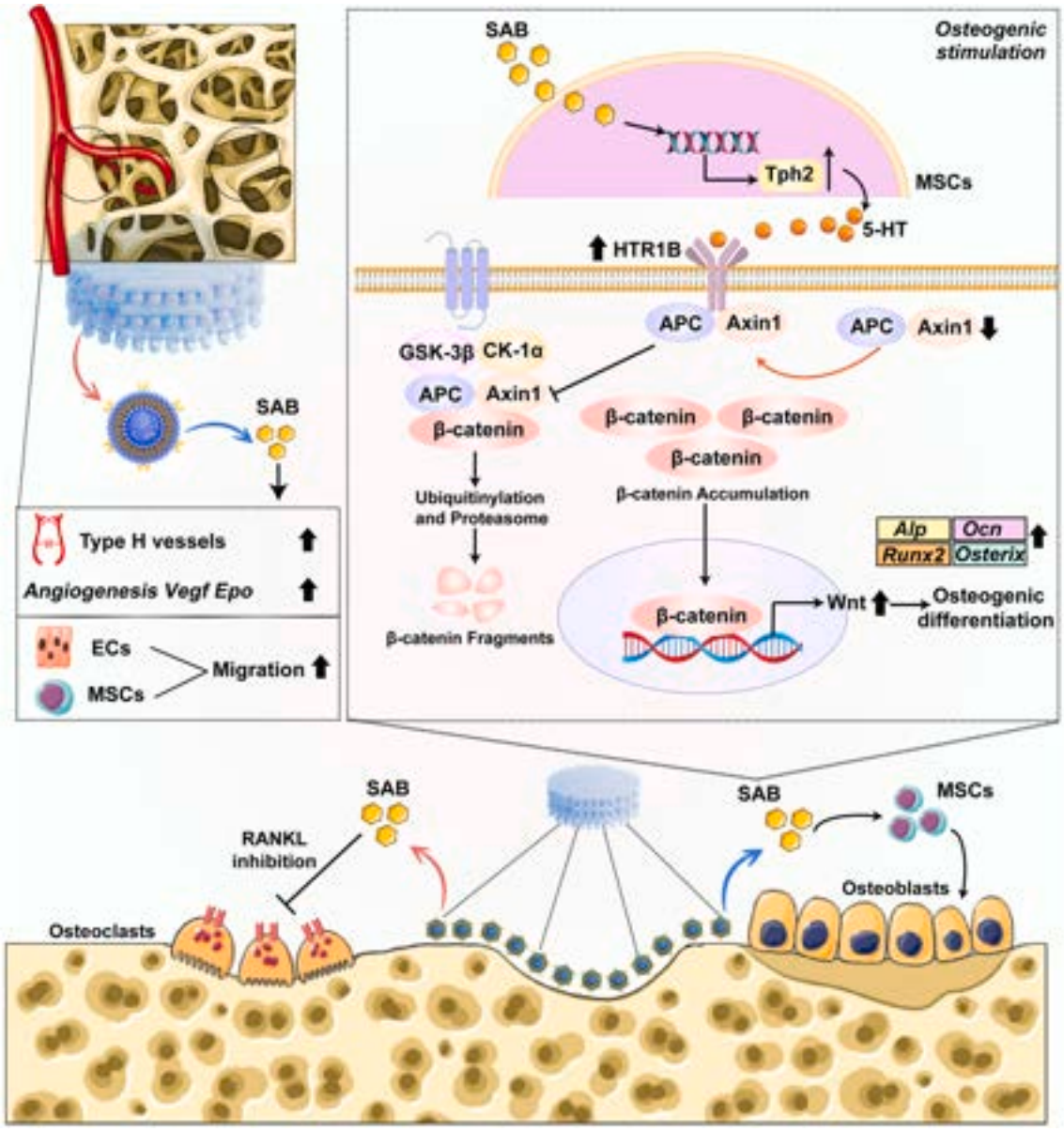

Fig. 9. Potential mechanism of APS@P scaffold treatment for OBD. The APS@P scaffold integrates SAB-BTL within an alginate/ε-polylysine scaffold, allowing for sustained drug release, targeted delivery, drug protection, and enhanced therapeutic efficacy. The therapeutic mechanism of APS@P in treating OBD involves several key processes: 1. Osteogenic Differentiation, APS@P promotes the osteogenic differentiation of mesenchymal stem cells (MSCs) by activating the Tph2/Wnt/β-catenin signaling axis. This activation leads to the upregulation of osteogenic biomarkers, including *Alp*, *Ocn*, *Runx2*, and *Osterix*. 2. Angiogenesis Promotion, the scaffold enhances angiogenesis through increased expression of vascular endothelial growth factor (*Vegf*) and erythropoietin (*Epo*). Additionally, it stimulates the formation of type H vessels, marked by co-expression of CD31 and endomucin, which are crucial for bone regeneration. 3. Inhibition of Bone Resorption, APS@P suppresses RANKL-mediated bone resorption, a key process in maintaining bone mass. These combined actions create a favorable microenvironment that restores bone homeostasis and promotes bone regeneration in OBD.

OBD (Fig. 9).

Unlike current drug therapies such as bisphosphonates, hormone replacement therapy, and RANKL inhibitors [71,72], our strategy provides more localized, targeted, and sustained drug delivery, which may result in improved therapeutic outcomes with minimizing systemic side effects. The APS@P scaffold system offers several key advantages that make it highly promising: **i)** By incorporating a bioactive drug for OBD, our obtained APS@P scaffold demonstrates a unique dual-regulatory function by simultaneously enhancing osteogenesis and suppressing bone resorption, offering a more comprehensive approach to addressing the imbalance. Given that very few drugs exhibit such bidirectional effects, SAB's incorporation into the scaffold significantly enhances its therapeutic potential. It not only enhances osteogenesis but also suppresses osteoclast activity and supports the formation of type H vessels, thereby promoting overall bone homeostasis and improving the regenerative potential for OBD repair. This multifunctional capability addresses a critical challenge in reversing dysregulated bone homeostasis of OBD. It also makes APS@P particularly well-suited for patients with complex bone defects, including those who have not responded well to conventional treatments, experience delayed or nonunion fractures, or face fixation challenges due to extensive bone damage. **ii)** our presented electrostatic encapsulation approach offers a unique solution by employing an electrostatic "sandwich structure" to enhance sustained and controlled drug release. This method is straightforward and does not require complex chemical modifications. Our *in vitro* release data confirmed a long-term sustained and stable SAB release, ensuring adequate amounts of bioactive factors remain available for supporting long-term bone repair. In addition, our system offers significant protection for unstable bioactive factors, shielding them from degradation or oxidation and thereby preserving their long-term efficacy. This makes the system especially well-suited for potent drugs prone to oxidation or degradation, thereby extending their efficacy and broadening their application for OBD treatment. **iii)** the bone-targeting liposomal formulation of SAB was also designed in the APS@P scaffold, for improving the drug accumulation in bone tissue, thereby enhancing localized drug delivery. This targeted delivery is crucial for osteoporotic defect repair, where localized treatment is necessary for effective osteointegration. Importantly, the drug-targeting strategy in our system does not require any modification of the drug itself, making it highly versatile and adaptable for loading a wide variety of therapeutic agents into 3D-printed scaffolds.

While our findings highlight the potential of the APS@P system, several challenges must be addressed before clinical application. A key issue is the scalability of scaffold production, where ensuring consistent quality, structural integrity, and therapeutic efficacy in large-scale manufacturing is critical. Additionally, while SAB demonstrated promising efficacy in our study, potential long-term side effects, especially with prolonged use, require thorough investigation. We acknowledge that the full mechanisms underlying the APS@P scaffold's function have not been completely elucidated, and further studies are needed to address this. Future research should focus on refining the scalability of APS@P production to ensure consistent quality and functionality for clinical use. It is equally important to evaluate the scaffold's long-term biocompatibility and *in vivo* efficacy. Moreover, optimizing its composition and mechanical properties, as well as exploring the potential benefits of combining APS@P with other bioactive molecules or stem cells, could enhance therapeutic outcomes. Expanding its application to various clinical contexts, such as traumatic bone injuries, congenital deformities, and bone tumors, would also be valuable. By tackling these challenges and broadening the scope of investigation, the APS@P system could represent a significant advancement in treating a range of bone-related conditions.

4. Conclusion

The APS@P scaffold, utilizing electrostatic encapsulation and a BTL strategy, successfully achieved stable and precise delivery of SAB, significantly enhancing its therapeutic efficacy in treating OBD. APS@P demonstrated multiple critical effects, including promoting osteogenesis, stimulating angiogenesis and cell migration, and inhibiting osteoclastogenesis—key processes for restoring bone homeostasis in OBD. Additionally, our study revealed that SAB's osteogenic effects are closely linked to the upregulation of the Tph2/Wnt/β-catenin signaling pathway. These findings highlight the feasibility and effectiveness of this treatment approach, offering strong empirical support for advanced OBD therapies. Moreover, the combination of electrostatic encapsulation and BTL strategies not only enhances the therapeutic potential of drug-loaded scaffolds, but also provides a versatile platform for delivering bioactive factors, advancing bone regeneration treatments.

5. Ethics approval and consent to participate

All experimental procedures were conducted in strict accordance with the guidelines of the "Guide for the Care and Use of Laboratory Animals" issued by both the Guangdong Laboratory Animal Monitoring Institute and the National Laboratory Animal Monitoring Institute of China. These procedures were performed under protocols approved by the Specific Pathogen-Free animal care unit of the Animal Center at Zhanjiang Central Hospital, Guangdong Medical University, with Laboratory Animal Use Permit Number SYXK(Guangdong)2023-0335. The Academic Committee on the Experimental Animal Ethics Committee of Zhanjiang Central Hospital, Zhanjiang, P.R. China, also approved these procedures under Permit Number ZJDY2023-01.

CRediT authorship contribution statement

Xiang Gao: Writing – original draft, Methodology. **Jirong Yang:** Writing – review & editing, Writing – original draft, Methodology, Funding acquisition. **Lingna Liu:** Writing – original draft, Methodology. **Zilong Hu:** Methodology. **Rui Lin:** Methodology, Formal analysis. **Lan Tang:** Data curation. **Mei Yu:** Methodology. **Zhiping Chen:** Validation. **Chongjian Gao:** Methodology. **Min Zhang:** Methodology. **Li Li:** Supervision, Project administration. **Changshun Ruan:** Writing – review & editing, Conceptualization. **Yanzhi Liu:** Writing – review & editing, Supervision, Investigation, Funding acquisition, Conceptualization.

Data availability statement

The data that support the findings of this study are available from the corresponding author upon reasonable request.

Funding sources

This research was funded by grants from National Key R&D Program (No. 2022YFB3804403), the National Natural Science Foundation of China (No. 92468106), Guangdong Basic and Applied Basic Research Foundation (Nos. 2024B1515040018, 2022A1515220166, 2023A1515011091, 2022A1515140138), the Science and Technology Foundation of Zhanjiang (Nos. 2022A01099, 2022A01163, 2022A01170), the Shenzhen Medical Research Fund (No. A2303016), the Shenzhen Science and Technology Program (No. JSGGKQTD20210831174330015, JCYJ20210324113001005), Discipline construction project of Guangdong Medical University (Nos. 4SG23002G and CLP2021B012), the Discipline Construction Fund of Central People's Hospital of Zhanjiang (No. 2022A09), Guangdong medical university research fund (No. FYZM001).

Declaration of competing interest

The authors declare no conflict of interest.

Appendix A. Supplementary data

Supplementary data to this article can be found online at https://doi.org/10.1016/j.bioactmat.2024.12.007.

References

[1] T.-L. Yang, H. Shen, A. Liu, S.-S. Dong, L. Zhang, F.-Y. Deng, et al., A road map for understanding molecular and genetic determinants of osteoporosis, Nat. Rev. Endocrinol. 16 (2020) 91–103, https://doi.org/10.1038/s41574-019-0282-7.

[2] M. Chen, D. Wang, M. Li, Y. He, T. He, M. Chen, et al., Nanocatalytic biofunctional MOF coating on titanium implants promotes osteoporotic bone regeneration through cooperative pro-osteoblastogenesis MSC reprogramming, ACS Nano 16 (2022) 15397–15412, https://doi.org/10.1021/acsnano.2c07200.

[3] F. Han, Z. Liu, Q. Wei, L. Ding, L. Yu, J. Wang, et al., Minimally invasive implantable biomaterials for bone reconstruction, Engineering (2024), https://doi.org/10.1016/j.eng.2024.01.031, 10.1016/j.eng.2024.01.031.

[4] J. Yang, X. Guo, Z. Cui, H. Guo, J.-N. Dong, Efficacy and safety of denosumab and teriparatide versus oral bisphosphonates to treat postmenopausal osteoporosis: a systematic review and meta-analysis, Front. Endocrinol. 15 (2024), https://doi.org/10.3389/fendo.2024.1431676.

[5] X. Chen, Y. Hu, Z. Geng, J. Su, The "three in one" bone repair strategy for osteoporotic fractures, Front. Endocrinol. 13 (2022), https://doi.org/10.3389/fendo.2022.910602.

[6] C. Yan, P. Zhang, Q. Qin, K. Jiang, Y. Luo, C. Xiang, et al., 3D-printed bone regeneration scaffolds modulate bone metabolic homeostasis through vascularization for osteoporotic bone defects, Biomaterials 311 (2024) 122699, https://doi.org/10.1016/j.biomaterials.2024.122699.

[7] D. Patel, S. Wairkar, Bone regeneration in osteoporosis: opportunities and challenges, Drug Delivery and Translational Research 13 (2023) 419–432, https://doi.org/10.1007/s13346-022-01222-6.

[8] T. Hoenig, K.E. Ackerman, B.R. Beck, M.L. Bouxsein, D.B. Burr, K. Hollander, et al., Bone stress injuries, Nat. Rev. Dis. Prim. 8 (2022) 26, https://doi.org/10.1038/s41572-022-00352-y.

[9] T. Song, J. Yang, P. Liu, M. Liu, D. Li, Y. Xiao, et al., Icariin self-crosslinked network functionalized strontium-doped bioceramic scaffolds synergistically enhanced the healing of osteoporotic bone defects, Compos. B Eng. 235 (2022) 109759, https://doi.org/10.1016/j.compositesb.2022.109759.

[10] J. Yang, Z. Chen, C. Gao, J. Liu, K. Liu, X. Wang, et al., A mechanical-assisted post-bioprinting strategy for challenging bone defects repair, Nat. Commun. 15 (2024) 3565, https://doi.org/10.1038/s41467-024-48023-8.

[11] J. Yang, H. He, D. Li, Q. Zhang, L. Xu, C. Ruan, Advanced strategies in the application of gelatin-based bioink for extrusion bioprinting, Bio-Design and Manufacturing 6 (2023) 586–608, https://doi.org/10.1007/s42242-023-00236-4.

[12] C. Vaquette, J. Mitchell, T. Fernandez-Medina, S. Kumar, S. Ivanovski, Resorbable additively manufactured scaffold imparts dimensional stability to extrasketetally regenerated bone, Biomaterials 269 (2021) 120671, https://doi.org/10.1016/j.biomaterials.2021.120671.

[13] W. Cheng, Y. Liu, X. Meng, Z. Zheng, L. Li, L. Ke, et al., PLGA/beta-TCP composite scaffold incorporating cucurbitacin B promotes bone regeneration by inducing angiogenesis, J Orthop Translat 31 (2021) 41–51, https://doi.org/10.1016/j.jot.2021.10.002.

[14] G.S. Shi, Y.Y. Li, Y.P. Luo, J.F. Jin, Y.X. Sun, L.Z. Zheng, et al., Bioactive PLGA/tricalcium phosphate scaffolds incorporating phytomolecule icaritin developed for calvarial defect repair in rat model, J Orthop Translat 24 (2020) 112–120, https://doi.org/10.1016/j.jot.2020.05.008.

[15] Y. Zhang, T. Lin, H. Meng, X. Wang, H. Peng, G. Liu, et al., 3D gel-printed porous magnesium scaffold coated with dibasic calcium phosphate dihydrate for bone repair in vivo, J Orthop Translat 33 (2022) 13–23, https://doi.org/10.1016/j.jot.2021.11.005.

[16] B. Wei, W. Wang, X. Liu, C. Xu, Y. Wang, Z. Wang, et al., Gelatin methacrylate hydrogel scaffold carrying resveratrol-loaded solid lipid nanoparticles for enhancement of osteogenic differentiation of BMSCs and effective bone regeneration, Regen Biomater 8 (2021) rbab044, https://doi.org/10.1093/rb/rbab044.

[17] B. Fang, P. Qiu, C. Xia, D. Cai, C. Zhao, Y. Chen, et al., Extracellular matrix scaffold crosslinked with vancomycin for multifunctional antibacterial bone infection therapy, Biomaterials 268 (2021) 120603, https://doi.org/10.1016/j.biomaterials.2020.120603.

[18] W. Zhang, W. Shi, S. Wu, M. Kuss, X. Jiang, J.B. Untrauer, et al., 3D printed composite scaffolds with dual small molecule delivery for mandibular bone regeneration, Biofabrication 12 (2020) 035020, https://doi.org/10.1088/1758-5090/ab906e.

[19] E.J. Sheehy, G.J. Miller, I. Amado, R.M. Raftery, G. Chen, K. Cortright, et al., Mechanobiology-informed regenerative medicine: dose-controlled release of placental growth factor from a functionalized collagen-based scaffold promotes angiogenesis and accelerates bone defect healing, J. Contr. Release 334 (2021) 96–105, https://doi.org/10.1016/j.jconrel.2021.03.031.

[20] X. Zhou, Y. Qian, L. Chen, T. Li, X. Sun, X. Ma, et al., Flowerbed-inspired biomimetic scaffold with rapid internal tissue infiltration and vascularization capacity for bone repair, ACS Nano 17 (2023) 5140–5156, https://doi.org/10.1021/acsnano.3c00598.

[21] Q. Zhang, J. Yang, N. Hu, J. Liu, H. Yu, H. Pan, et al., Small-molecule amines: a big role in the regulation of bone homeostasis, Bone Res 11 (2023) 40, https://doi.org/10.1038/s41413-023-00262-z.

[22] Y. Zhao, H. Kang, X. Wu, P. Zhuang, R. Tu, T. Goto, et al., Multifunctional scaffold for osteoporotic pathophysiological microenvironment improvement and vascularized bone defect regeneration, Adv. Healthcare Mater. 12 (2023) 2203099, https://doi.org/10.1002/adhm.202203099.

[23] Z. Ye, Y. Liu, J. Song, Y. Gao, H. Fang, Z. Hu, et al., Expanding the therapeutic potential of Salvia miltiorrhiza: a review of its pharmacological applications in musculoskeletal diseases, Front. Pharmacol. 14 (2023) 1276038, https://doi.org/10.3389/fphar.2023.1276038.

[24] L. Cui, T. Li, Y. Liu, L. Zhou, P. Li, B. Xu, et al., Salvianolic acid B prevents bone loss in prednisone-treated rats through stimulation of osteogenesis and bone marrow angiogenesis, PLoS One 7 (2012) e34647, https://doi.org/10.1371/journal.pone.0034647.

[25] S.Y. Luo, J.F. Chen, Z.G. Zhong, X.H. Lv, Y.J. Yang, J.J. Zhang, et al., Salvianolic acid B stimulates osteogenesis in dexamethasone-treated zebrafish larvae, Acta Pharmacol. Sin. 37 (2016) 1370–1380, https://doi.org/10.1038/aps.2016.62.

[26] J. Qiao, A. Liu, J. Liu, D. Guan, T. Chen, Salvianolic acid B (Sal B) alleviates the decreased activity induced by prednisolone acetate on osteoblasts by up-regulation of bone formation and differentiation genes, Food Funct. 10 (2019) 6184–6192, https://doi.org/10.1039/c9fo01246j.

[27] S. Lin, L. Cui, G. Chen, J. Huang, Y. Yang, K. Zou, et al., PLGA/beta-TCP composite scaffold incorporating salvianolic acid B promotes bone fusion by angiogenesis and osteogenesis in a rat spinal fusion model, Biomaterials 196 (2019) 109–121, https://doi.org/10.1016/j.biomaterials.2018.04.004.

[28] W. Wang, Y. Liu, C. Yang, W. Jia, X. Qi, C. Liu, et al., Delivery of salvianolic acid B for efficient osteogenesis and angiogenesis from silk fibroin combined with graphene oxide, ACS Biomater. Sci. Eng. 6 (2020) 3539–3549, https://doi.org/10.1021/acsbiomaterials.0c00558.

[29] X. Gao, Q. Wu, X. Zhang, J. Tian, D. Liang, Y. Min, et al., Salvianolate ameliorates osteopenia and improves bone quality in prednisone-treated rheumatoid arthritis rats by regulating RANKL/RANK/OPG signaling, Front. Pharmacol. 12 (2021) 710169, https://doi.org/10.3389/fphar.2021.710169.

[30] Y. Tang, A. Jacobi, C. Vater, X. Zou, M. Stiehler, Salvianolic acid B protects human endothelial progenitor cells against oxidative stress-mediated dysfunction by modulating Akt/mTOR/4EBP1, p38 MAPK/ATF2, and ERK1/2 signaling pathways, Biochem. Pharmacol. 90 (2014) 34–49, https://doi.org/10.1016/j.bcp.2014.04.008.

[31] D. Xu, L. Xu, C. Zhou, W.Y. Lee, T. Wu, L. Cui, et al., Salvianolic acid B promotes osteogenesis of human mesenchymal stem cells through activating ERK signaling pathway, Int. J. Biochem. Cell Biol. 51 (2014) 1–9, https://doi.org/10.1016/j.biocel.2014.03.005.

[32] Y. Bian, J. Xiang, Salvianolic acid B promotes the osteogenic differentiation of human periodontal ligament cells through Wnt/beta-catenin signaling pathway, Arch. Oral Biol. 113 (2020) 104693, https://doi.org/10.1016/j.archoralbio.2020.104693.

[33] L. Cui, Y.Y. Liu, T. Wu, C.M. Ai, H.Q. Chen, Osteogenic effects of D+beta-3,4-dihydroxyphenyl lactic acid (salvianic acid A, SAA) on osteoblasts and bone marrow stromal cells of intact and prednisone-treated rats, Acta Pharmacol. Sin. 30 (2009) 321–332, https://doi.org/10.1038/aps.2009.9.

[34] Y. Yang, Y. Su, D. Wang, Y. Chen, T. Wu, G. Li, et al., Tanshinol attenuates the deleterious effects of oxidative stress on osteoblastic differentiation via Wnt/FoxO3a signaling, Oxid. Med. Cell. Longev. 2013 (2013) 351895, https://doi.org/10.1155/2013/351895.

[35] W. Lai, Y. Mo, D. Wang, Y. Zhong, L. Lu, J. Wang, et al., Tanshinol alleviates microcirculation disturbance and impaired bone formation by attenuating TXNIP signaling in GIO rats, Front. Pharmacol. 12 (2021) 722175, https://doi.org/10.3389/fphar.2021.722175.

[36] Y.J. Yang, Z. Zhu, D.T. Wang, X.L. Zhang, Y.Y. Liu, W.X. Lai, et al., Tanshinol alleviates impaired bone formation by inhibiting adipogenesis via KLF15/PPARgamma2 signaling in GIO rats, Acta Pharmacol. Sin. 39 (2018) 633–641, https://doi.org/10.1038/aps.2017.134.

[37] B. Xiao, Y. Liu, I. Chandrasiri, E. Adjei-Sowah, J. Mereness, M. Yan, et al., Bone-targeted nanoparticle drug delivery system-mediated macrophage modulation for enhanced fracture healing, Small 20 (2024) e2305336, https://doi.org/10.1002/smll.202305336.

[38] Y. He, L. Zhang, X. Chen, B. Liu, X. Shao, D. Fang, et al., Elimination of senescent osteocytes by bone-targeting delivery of beta-galactose-modified maytansinoid prevents age-related bone loss, Adv. Healthcare Mater. 13 (2024) e2302972, https://doi.org/10.1002/adhm.202302972.

[39] Y. Liu, Z. Jia, M.P. Akhter, X. Gao, X. Wang, X. Wang, et al., Bone-targeting liposome formulation of Salvianic acid A accelerates the healing of delayed fracture Union in Mice, Nanomedicine 14 (2018) 2271–2282, https://doi.org/10.1016/j.nano.2018.07.011.

[40] L. Zhou, H. Wu, X. Gao, X. Zheng, H. Chen, H. Li, et al., Bone-targeting liposome-encapsulated salvianic acid A improves nonunion healing through the regulation of HDAC3-mediated endochondral ossification, Drug Des. Dev. Ther. 14 (2020) 3519–3533, https://doi.org/10.2147/DDDT.S263787.

[41] Y. Liu, Z. Jia, L. Ma, D. Wang, Pyrophosphorylated-cholesterol-modified bone-targeting liposome formulation procedure, in: G.G.M. D'Souza, H. Zhang (Eds.), Liposomes: Methods and Protocols, Springer US, New York, NY, 2023, pp. 207–220.

[42] Z. Lin, M. Wu, H. He, Q. Liang, C. Hu, Z. Zeng, et al., 3D printing of mechanically stable calcium-free alginate-based scaffolds with tunable surface charge to enable

cell adhesion and facile biofunctionalization, Adv. Funct. Mater. 29 (2019) 1808439, https://doi.org/10.1002/adfm.201808439.
[43] L. Cui, T. Li, Y. Liu, L. Zhou, P. Li, B. Xu, et al., Salvianolic acid B prevents bone loss in prednisone-treated rats through stimulation of osteogenesis and bone marrow angiogenesis, PLoS One 7 (2012) e34647, https://doi.org/10.1371/journal.pone.0034647.
[44] J. Song, Y. Ju, T.H. Amarasena, Z. Lin, S. Mettu, J. Zhou, et al., Influence of poly (ethylene glycol) molecular architecture on particle assembly and ex vivo particle–immune cell interactions in human blood, ACS Nano 15 (2021) 10025–10038, https://doi.org/10.1021/acsnano.1c01642.
[45] Q. Chen, L. Yuan, W.-C. Chou, Y.-H. Cheng, C. He, N.A. Monteiro-Riviere, et al., Meta-analysis of nanoparticle distribution in tumors and major organs in tumor-bearing mice, ACS Nano 17 (2023) 19810–19831, https://doi.org/10.1021/acsnano.3c04037.
[46] J. Vanderburgh, J.L. Hill, M.K. Gupta, K.A. Kwakwa, S.K. Wang, K. Moyer, et al., Tuning ligand density to optimize pharmacokinetics of targeted nanoparticles for dual protection against tumor-induced bone destruction, ACS Nano 14 (2020) 311–327, https://doi.org/10.1021/acsnano.9b04571.
[47] L. Lu, L. Lu, J. Zhang, J. Li, Potential risks of rare serious adverse effects related to long-term use of bisphosphonates: an overview of systematic reviews, J. Clin. Pharm. Therapeut. 45 (2020) 45–51, https://doi.org/10.1111/jcpt.13056.
[48] Y. Zhao, H. Kang, X. Wu, P. Zhuang, R. Tu, T. Goto, et al., Multifunctional scaffold for osteoporotic pathophysiological microenvironment improvement and vascularized bone defect regeneration, Adv. Healthcare Mater. 12 (2023) e2203099, https://doi.org/10.1002/adhm.202203099.
[49] C.I. Codrea, A.M. Croitoru, C.C. Baciu, A. Melinescu, D. Ficai, V. Fruth, et al., Advances in osteoporotic bone tissue engineering, J. Clin. Med. 10 (2021), https://doi.org/10.3390/jcm10020253.
[50] P. Kangari, T. Talaei-Khozani, I. Razeghian-Jahromi, M. Razmkhah, Mesenchymal stem cells: amazing remedies for bone and cartilage defects, Stem Cell Res. Ther. 11 (2020) 492, https://doi.org/10.1186/s13287-020-02001-1.
[51] H. Lin, J. Sohn, H. Shen, M.T. Langhans, R.S. Tuan, Bone marrow mesenchymal stem cells: aging and tissue engineering applications to enhance bone healing, Biomaterials 203 (2019) 96–110, https://doi.org/10.1016/j.biomaterials.2018.06.026.
[52] Z. Xu, A.P. Kusumbe, H. Cai, Q. Wan, J. Chen, Type H blood vessels in coupling angiogenesis-osteogenesis and its application in bone tissue engineering, J. Biomed. Mater. Res. B Appl. Biomater. 111 (2023) 1434–1446, https://doi.org/10.1002/jbm.b.35243.
[53] B. Wildemann, A. Ignatius, F. Leung, L.A. Taitsman, R.M. Smith, R. Pesantez, et al., Non-union bone fractures, Nat. Rev. Dis. Prim. 7 (2021) 57, https://doi.org/10.1038/s41572-021-00289-8.
[54] S. Lin, L. Cui, G. Chen, J. Huang, Y. Yang, K. Zou, et al., PLGA/beta-TCP composite scaffold incorporating salvianolic acid B promotes bone fusion by angiogenesis and osteogenesis in a rat spinal fusion model, Biomaterials (2018), https://doi.org/10.1016/j.biomaterials.2018.04.004, 10.1016/j.biomaterials.2018.04.004.
[55] C. Ji, L. Bi, J. Li, J. Fan, Salvianolic acid B-loaded chitosan/hydroxyapatite scaffolds promotes the repair of segmental bone defect by angiogenesis and osteogenesis, Int. J. Nanomed. 14 (2019) 8271–8284, https://doi.org/10.2147/IJN.S219105.
[56] J. Chen, Y. Wang, S. Wang, X. Zhao, L. Zhao, Y. Wang, Salvianolic acid B and ferulic acid synergistically promote angiogenesis in HUVECs and zebrafish via regulating VEGF signaling, J. Ethnopharmacol. 283 (2022) 114667, https://doi.org/10.1016/j.jep.2021.114667.
[57] Q. Chen, Q. Xu, H. Zhu, J. Wang, N. Sun, H. Bian, et al., Salvianolic acid B promotes angiogenesis and inhibits cardiomyocyte apoptosis by regulating autophagy in myocardial ischemia, Chin. Med. 18 (2023) 155, https://doi.org/10.1186/s13020-023-00859-w.
[58] X. Li, R. Liu, W. Liu, X. Liu, Z. Fan, J. Cui, et al., Panax quinquefolium L. And Salvia miltiorrhiza bunge. Enhances angiogenesis by regulating the miR-155-5p/HIF-1alpha/VEGF Axis in acute myocardial infarction, Drug Des. Dev. Ther. 17 (2023) 3249–3267, https://doi.org/10.2147/DDDT.S426345.
[59] M.X. Zhang, X.Y. Huang, Y. Song, W.L. Xu, Y.L. Li, C. Li, Astragalus propinquus schischkin and Salvia miltiorrhiza bunge promote angiogenesis to treat myocardial ischemia via Ang-1/Tie-2/FAK pathway, Front. Pharmacol. 13 (2022) 1103557, https://doi.org/10.3389/fphar.2022.1103557.
[60] G.N. Duda, S. Geissler, S. Checa, S. Tsitsilonis, A. Petersen, K. Schmidt-Bleek, The decisive early phase of bone regeneration, Nat. Rev. Rheumatol. 19 (2023) 78–95, https://doi.org/10.1038/s41584-022-00887-0.
[61] N. Yousefzadeh, K. Kashfi, S. Jeddi, A. Ghasemi, Ovariectomized rat model of osteoporosis: a practical guide, EXCLI J 19 (2020) 89–107, https://doi.org/10.17179/excli2019-1990.
[62] T. Iwasa, T. Matsuzaki, K. Yano, M. Irahara, The effects of ovariectomy and lifelong high-fat diet consumption on body weight, appetite, and lifespan in female rats, Horm. Behav. 97 (2018) 25–30, https://doi.org/10.1016/j.yhbeh.2017.10.005.
[63] Y. Peng, S. Wu, Y. Li, J.L. Crane, Type H blood vessels in bone modeling and remodeling, Theranostics 10 (2020) 426–436, https://doi.org/10.7150/thno.34126.
[64] Y. Liu, L. Cao, S. Ray, U. Thormann, J. Hillengass, S. Delorme, et al., Osteoporosis influences osteogenic but not angiogenic response during bone defect healing in a rat model, Injury 44 (2013) 923–929, https://doi.org/10.1016/j.injury.2013.02.029.
[65] V.K. Yadav, F. Oury, N. Suda, Z.W. Liu, X.B. Gao, C. Confavreux, et al., A serotonin-dependent mechanism explains the leptin regulation of bone mass, appetite, and energy expenditure, Cell 138 (2009) 976–989, https://doi.org/10.1016/j.cell.2009.06.051.
[66] Y. Zhao, X. Peng, Q. Wang, Z. Zhang, L. Wang, Y. Xu, et al., Crosstalk between the neuroendocrine system and bone homeostasis, Endocr. Rev. 45 (2023) 95–124, https://doi.org/10.1210/endrev/bnad025.
[67] R. Vlashi, X. Zhang, M. Wu, G. Chen, Wnt signaling: essential roles in osteoblast differentiation, bone metabolism and therapeutic implications for bone and skeletal disorders, Genes & diseases 10 (2023) 1291–1317, https://doi.org/10.1016/j.gendis.2022.07.011.
[68] P. Zhu, T. Lu, Z. Chen, B. Liu, D. Fan, C. Li, et al., 5-hydroxytryptamine produced by enteric serotonergic neurons initiates colorectal cancer stem cell self-renewal and tumorigenesis, Neuron 110 (2022), https://doi.org/10.1016/j.neuron.2022.04.024, 2268-22682 e4.
[69] J. Chen, B. Tschudy-Seney, X. Ma, M.A. Zern, P. Liu, Y. Duan, Salvianolic acid B enhances hepatic differentiation of human embryonic stem cells through upregulation of WNT pathway and inhibition of Notch pathway, Stem Cell. Dev. 27 (2018) 252–261, https://doi.org/10.1089/scd.2017.0168.
[70] T. Shu, C. Liu, M. Pang, L. He, B. Yang, L. Fan, et al., Salvianolic acid B promotes neural differentiation of induced pluripotent stem cells via PI3K/AKT/GSK3beta/beta-catenin pathway, Neurosci. Lett. 671 (2018) 154–160, https://doi.org/10.1016/j.neulet.2018.02.007.
[71] I. Foessl, H.P. Dimai, B. Obermayer-Pietsch, Long-term and sequential treatment for osteoporosis, Nat. Rev. Endocrinol. 19 (2023) 520–533, https://doi.org/10.1038/s41574-023-00866-9.
[72] A. Qaseem, L.A. Hicks, I. Etxeandia-Ikobaltzeta, T. Shamliyan, T.G. Cooney, Clinical Guidelines Committee of the American College of P, et al., Pharmacologic treatment of primary osteoporosis or low bone mass to prevent fractures in adults: a living clinical guideline from the American college of physicians, Ann. Intern. Med. 176 (2023) 224–238, https://doi.org/10.7326/M22-1034.